REPORT DOCUMENTATION PAGE

1. REPORT DATE (DD-MM-YYYY)	2. REPORT TYPE	3. DATES COVERED (From - To)
31-12-2012	Final Report	1 Oct 09 - 31 Aug 12

4. TITLE AND SUBTITLE

Photonic Materials and Devices for RF (mmW) Sensing and Imaging

5a. CONTRACT NUMBER

5b. GRANT NUMBER

N00014-10-1-0176

5c. PROGRAM ELEMENT NUMBER

6. AUTHOR(S)

Prather, Dennis W.

5d. PROJECT NUMBER

5e. TASK NUMBER

5f. WORK UNIT NUMBER

7. PERFORMING ORGANIZATION NAME(S) AND ADDRESS(ES)

University of Delaware
210 Hullihen Hall
Newark, DE 19716

8. PERFORMING ORGANIZATION REPORT NUMBER

ELEG332271-062813

9. SPONSORING/MONITORING AGENCY NAME(S) AND ADDRESS(ES)

Office of Naval Research Regional Admin Atlanta
100 Alabama Street, SW Suite 4R15
Atlanta, GA 30303-3104

10. SPONSOR/MONITOR'S ACRONYM(S)

11. SPONSOR/MONITOR'S REPORT NUMBER(S)

12. DISTRIBUTION/AVAILABILITY STATEMENT

Distribution is unlimited.

13. SUPPLEMENTARY NOTES

14. ABSTRACT

Within the scope of previous efforts for ONR, the University of Delaware has developed and demonstrated a novel technique for imaging in the millimeter-wave spectrum without the use of traditional imaging optics. Efforts have been ongoing to develop a two dimensional array. However, the effective implementation of this technology is hampered by the availability of component technologies that, while critical to this effort, had not yet become commercially available. These technologies have not yet been developed for the most part due to a lack of a commodity market rather than significant technological barriers to entry. Under this effort, we have successfully developed these component technologies sufficiently to realize their use in the proposed optical upconversion imaging scheme. The component technologies developed under this effort include: packaged high-speed optical modulators, large area optical filters for carrier rejection, and 2-D fiber array geometries for distributed aperture optical synthesis. Using these components, both a W-band scanning, single-pixel imager and a Q-band interferometric imager have been fabricated.

15. SUBJECT TERMS

Passive millimeter-wave imaging, optical modulator, sparse aperture imaging

16. SECURITY CLASSIFICATION OF:			17. LIMITATION OF ABSTRACT	18. NUMBER OF PAGES	19a. NAME OF RESPONSIBLE PERSON
a. REPORT	b. ABSTRACT	c. THIS PAGE			Dennis W. Prather
U	U	U	UU	37	**19b. TELEPHONE NUMBER** (Include area code)
					302-831-8170

Reset

Photonic Materials and Devices for RF (mmW) Sensing and Imaging

Dennis W. Prather, Ph.D.

University of Delaware
Department of Electrical and Computer Engineering
140 Evans Hall, Room 108
Newark, DE, 19716-3130
Tel: (302)831-8170, Fax: (302)831-8172, Email: dprather@ee.udel.edu

ABSTRACT

Within the scope of previous efforts for ONR, the University of Delaware has developed and demonstrated a novel technique for imaging in the millimeter-wave spectrum without the use of traditional imaging optics. This technique is based on distributed aperture image reconstruction using optical upconversion. Previous efforts have yielded a successful demonstration of the technology for a one dimensional array. Efforts have been ongoing to develop a two dimensional array. However, the effective implementation of this technology is hampered by the availability of component technologies that, while critical to this effort, had not yet become commercially available. These technologies have not yet been developed for the most part due to a lack of a commodity market rather than significant technological barriers to entry. Under this effort, we have successfully developed these component technologies sufficiently to realize their use in the proposed optical upconversion imaging scheme. The component technologies developed under this effort include: packaged high-speed optical modulators, large area optical filters for carrier rejection, and 2-D fiber array geometries for distributed aperture optical synthesis. Using these components, both a W-band scanning, single-pixel imager and a Q-band interferometric imager have been fabricated.

INTRODUCTION

Millimeter waves (mmWs) are electromagnetic radiation with wavelengths in the range 1 cm to 1 mm (with corresponding frequencies of 30 to 300 GHz), and are located between the microwave and infrared portions of the spectrum. Because of their unique ability to penetrate fog, dust, smoke, and light rain, mmW imaging systems are very attractive in many military applications. In addition, mmW imaging presents many unique opportunities in the maritime

applications. In addition, mmW imaging presents many unique opportunities in the maritime environment due to the unique transmission properties in this range of the spectrum. Since terrestrial blackbody emission in this spectrum, while small, is becoming detectable with recent technology development, it is progressively enabling all-weather passive imaging in these bands. However, their use in military systems has been limited due to the lack of suitable technologies to meet and exceed the mission specific design criteria, e.g., resolution, field of view, sensitivity, and cost. While several mmW systems have been built, that serve to demonstrate their utility, they have not been widely used. The main reason for this is that in comparison to optical wavelengths, mmWs are 1,000 to 10,000 times larger, and as a result, the associated imaging elements and corresponding systems tend to be large, expensive, and inconvenient. Especially for military airborne applications, systems realized to date have been impractical. Distributed aperture techniques could open up a wider range of applications by mitigating the volume requirements of high resolution imagers. Unfortunately, traditional distributed aperture techniques encounter significant complications governed by the significant detection, routing, and processing requirements of such distributed arrays.

To circumvent this, we present an approach towards the realization of millimeter-wave, distributed-aperture imagers using optical techniques. By using electro-optic modulators to upconvert received millimeter-wave fields onto an optical carrier, such fields can be readily captured, routed, and processed using optical techniques, thereby providing significant advantages over more traditional heterodyne imagers. Prior to this effort, we had demonstrated a one-dimensional demonstration imager using these techniques. Under this effort, we realized component technologies necessary to create the full 2-D realization of this imaging modality necessary to create video rate imagery. These component technologies include large-area spectrally-sharp optical filters for carrier rejection and 2-D fiber array. In addition, these technologies have been incorporated into a prototype system operating at ~36 GHz, which has demonstrated the viability of this approach to creating millimeter-wave imagery. Finally, in a step towards realizing higher-resolution imagery, W-band optical modulators have been packaged and millimeter-wave imagery has been created using these modulators in a single-pixel scanning radiometer configuration. The details of both the components developed under this effort and the systems into which they have been installed are presented in further detail herein.

TECHNICAL BACKGROUND

The components developed under these efforts have been implemented in millimeter-wave imagers of two configurations: a distributed aperture imager based on optical upconversion and a single-pixel scanning system using an optical upconversion detector. These systems are described in detail below.

DISTRIBUTED APERTURE OVERVIEW

Traditional imaging techniques, such as focal plane arrays or scanned staring systems, require a volumetric increase in imager size and, subsequently, weight to improve imager resolution. Thus, such systems are largely impractical for many applications. Distributed

aperture approaches, which synthetically reproduce image data from an array of detectors are currently under development for millimeter-wave sounding applications. Image reconstruction for distributed imaging methodologies requires the capture of both magnitude and phase of millimeter-wave field at each element of the array. Additionally, captured field information must be post-processed with large correlation engines to recover the original scene. Current embodiments of distributed aperture imagers utilize distributed local oscillators and mixers to down-convert the captured field data to low intermediate frequency where it is digitally recorded. Subsequent cross-correlators are required to regenerate the image data.

Although, this approach shows significant promise for space-based microwave sounding imagery, several challenges are posed in the system design. First, local oscillator (LO) distribution requires phase stable delivery of the high frequency LO to sampling point of the array. For frequencies below ~67 GHz flexible coaxial cables may be used. However, such cables are bulky and of limited flexibility. At higher frequencies, the challenges posed by LO distribution become more severe, requiring either the use of inflexible metal waveguide or separate mixers for each node to generate the synchronized LO. Thus, LO distribution can significantly limit launch accommodation and deployment profiles available. The significant power, size, and space requirements of the mixer, IF processing and correlation engines also present significant challenges for systems integrators.
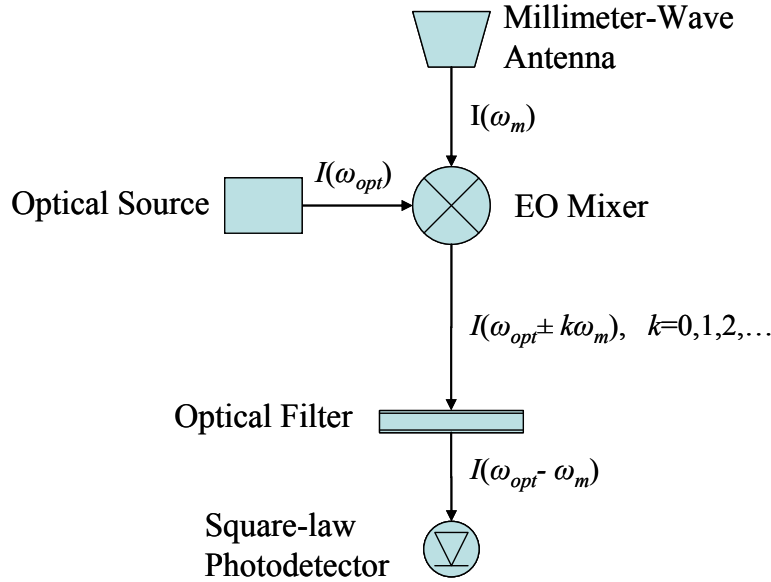
Millimeter-Wave Antenna

$I(\omega_m)$

Optical Source $\quad I(\omega_{opt}) \quad$ ⊗ EO Mixer

$I(\omega_{opt} \pm k\omega_m), \quad k=0,1,2,\dots$

Optical Filter

$I(\omega_{opt} - \omega_m)$

Square-law Photodetector

Figure 1. Single pixel realization of optically-based millimeter-wave detection process.

In this proposal we present an alternate approach to distributed aperture imaging for naval applications based on optical upconversion techniques. Unlike the common heterodyne downconversion techniques used in radiometers, our approach would use electro-optic modulation techniques to convert received millimeter-wave radiation into sidebands on an optical carrier. Such a technique maintains the benefits of distributed aperture approaches while providing many potential advantages over digital heterodyne correlation imaging. Optical upconversion allows for the use of lightweight, flexible fiber optics for the routing of optical

energy both before and after millimeter-wave encoding thereby eliminating the need for bulky LO distribution cables. Also, optical processing techniques can be utilized to provide simple correlation engines using simple optical lenses and cameras.

The heart of this process lies in the optical upconversion process, which is based on commercial electro-optic modulators. These modulators operate in a similar fashion to heterodyne mixers by shifting the millimeter-wave radiation to another frequency to ease processing while preserving both amplitude and phase information of the captured signal.

To verify the transfer of the complex millimeter-wave field to the optical domain, we must first examine the details of the optical modulation process. Electro-optic modulation converts energy into the sidebands by imposing a phase change, $\Delta\phi$, to the optical field proportional to the applied millimeter-wave field described by

$$\Delta\phi = mE_m \cos\left(\omega_m t + \phi_m\right), \tag{1}$$

where m is a modulation constant dependent on the properties of the modulator and the efficiency of the collection antenna, and E_m and ϕ_m are the strength and phase of the incident millimeter-wave field, respectively. Thus, the output field, E_o, of a the electro-optic modulator may be described as

$$E_o = E_{opt}\, \mathrm{e}^{j\omega_{opt}t + j\left(\Delta\phi + \phi_{opt}\right)} = E_{opt}\, \mathrm{e}^{j\omega_{opt}t + jmE_m \cos\left(\omega_m t + \phi_m\right)}, \tag{2}$$

where $E_{opt}\, exp(j\omega_{opt}t + \phi_{opt})$ describes the optical field incident on the modulator. Using Fourier expansion techniques and assuming a small, imposed millimeter-wave field the field strength of the imposed first-order sideband can be shown to be

$$E_{o,FSB} = \frac{jmE_{opt}}{2}\left(E_m\, \mathrm{e}^{j\left(\omega_{opt} + \omega_m\right)t + j\left(\phi_m + \phi_{opt}\right)} \right). \tag{3}$$

Equation (3) can be seen as nothing more than the initial complex millimeter-wave field scaled in amplitude by a factor $mE_{opt}/2$ and in wavelength by a factor $\omega_m/(\omega_{opt}+\omega_m)$. In addition, a phase component, due to the optical path length is included. Wavelength scaling allows smaller components such as fiber optic waveguides to replace bulky coaxial or metallic waveguides. The amplitude scaling, for reasonable optical powers, can be close to unity and low-noise photodetectors make the detection of exceedingly low power millimeter-waves practical. In previous work, we have shown that this technique can be used to create very sensitive millimeter-wave detectors as shown in Figure 2.1. By simply optically-filtering the modulated signal to pass only a single sideband and detecting the resultant optical signal with a low-noise photodetector we have demonstrated millimeter-wave detectors with NETD's as low as 1.5 K/$\sqrt{\mathrm{Hz}}$ without LNA's or cooling in both Q and W bands.

Perhaps an even more useful application of optical upconversion to millimeter-wave imagers comes from the benefits that can be obtained in distributed aperture imaging techniques. At the University of Delaware, we have demonstrated progress towards millimeter-wave synthetic aperture imaging implemented via a carrier-suppressed optical approach. The crux of such a technique relies on using the spatial Fourier Transform properties of an optical lens to perform the numerous correlations required to regenerate the image from the sampled u-v plane. In fact, digital correlation algorithms are essentially methods for performing discrete spatial

Fourier transforms. Such methods require increasingly numerous correlations ($\sim n^2/2$ correlations for n nodes) as the number of antenna nodes grows. Using the smaller optical wavelengths, Fourier transform operations may be carried out using a simple small optical lens and a photodetector array as shown in Figure 2.3. As such, the sampled image is generated in real time without the use of complicated correlation engines. Conceptually, this approach may be thought of as a technique for:

o Discretely sampling the complex amplitude of the millimeter-wave signal.
o Converting the captured complex amplitude to optical wavelengths.
o Routing upconverted signals to a central processor fiber array that mimics the MMW array format.
o Performing a continuous spatial Fourier transform of the discretely sampled aperture using simple optics at shorter wavelengths where the diffraction limit does not inhibit resolution.
o Capturing regenerated imagery in real time using a standard optical detector array.

We have already begun preliminary investigations into the fabricating such optically processed distributed aperture arrays. Initial results have successfully demonstrated 1-dimensional implementations of such an approach, which is described below.
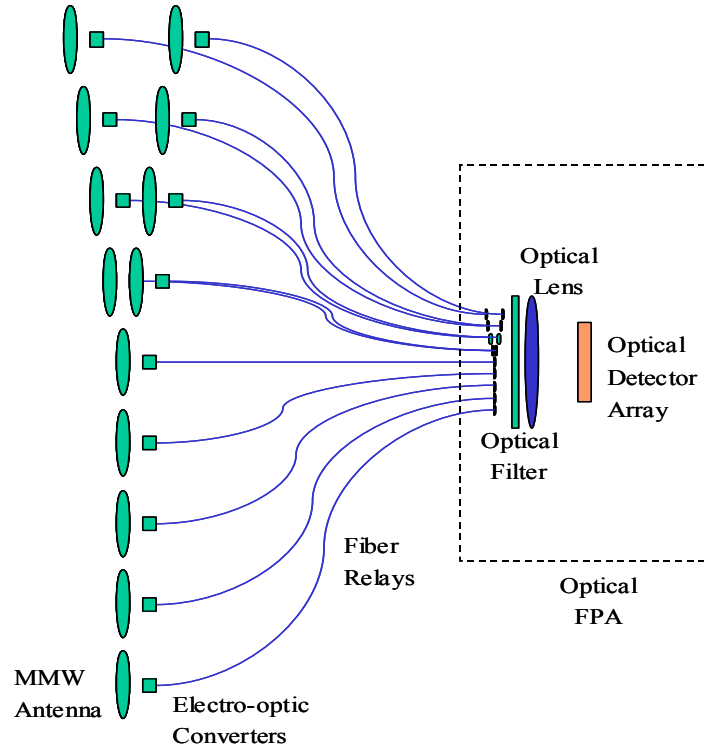

Figure 2. Schematic representation of optical processing techniques for distributed aperture arrays.

One critical element in deploying such optically based imagers is the control of optically induced phase variations. To maintain the phase coherence of the complex fields, each optical modulator must be fed from a single common optical source. Since the effective wavelength of the upconverted sidebands is on the order of 1μm, minor variations in path length due to thermal drift or acoustic noise can induce significant phase drifts over the sampled array. If left uncontrolled such phase variations would destroy the ability of the distributed array to create meaningful image data. One of the key aspects of our approach is that we have developed robust techniques to compensate for such phase drifts.

The optical modulation process only converts a small amount of the optical carrier into upconverted millimeter-wave energy. The remaining optical carrier travels an identical optical path as the encoded sidebands and, as such, experiences the same phase drifts induced by the optical path. Thus, the relative paths of each of the array samples can be compared to a single reference in the central processor to determine the optical phase error induced for each leg. Since the optical modulators at each node of the antenna array already include phase shifting techniques, known phase errors may be readily compensated for by means of an applied DC bias to the optical modulator. However,
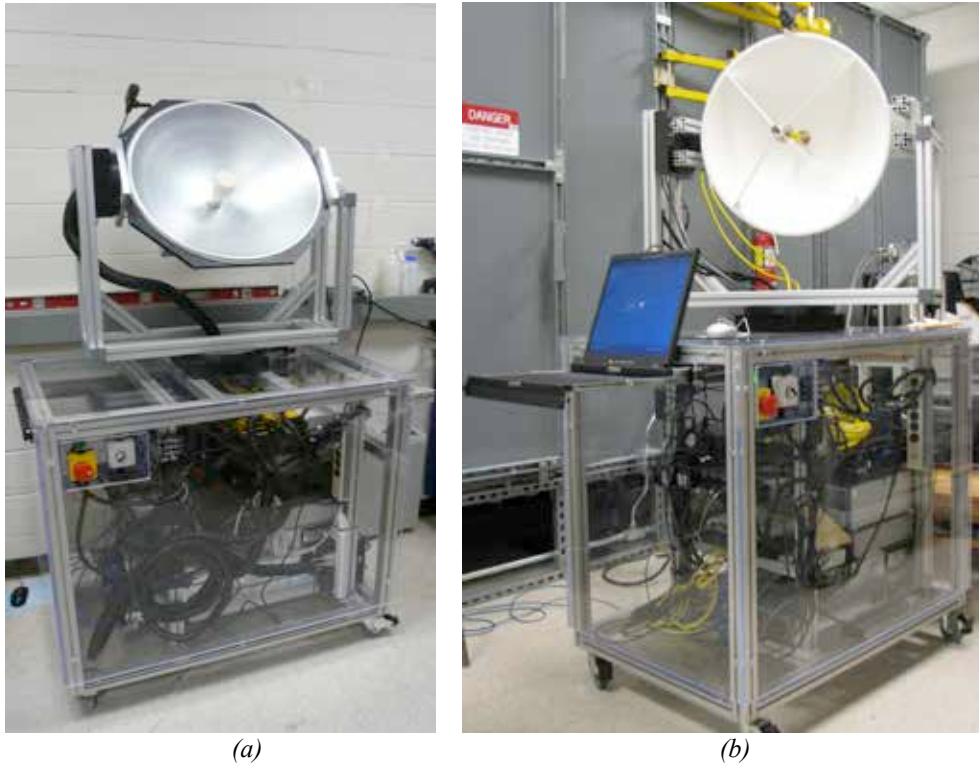
SINGLE-PIXEL SCANNING SYSTEM

(a)   *(b)*
Figure 3. (a) 35 GHz cart and (b) 94 GHz far-field imager cart.

6

To demonstrate the viability of optical upconversion as a passive millimeter-wave detection mechanism, the optical detector technology was used to create two single pixel imaging carts, one operating over Q-band (33-50 GHz) and one operating over W-band (75-110 GHz). *The modulator packaging efforts developed under this program were essential to the creation of the W-band cart*, which yields significantly higher resolution. These carts were used to investigate imaging phenomenology of interest in naval environments and were a key input to multiple perception studies, which provided the first empirical data regarding millimeter-wave imagery for achieving proscribed level of task performance. In particular, mmW imagery generated by these carts under a related effort was used to calculate N50 and V50 numbers for small watercraft identification in the millimeter-wave regime. The imager architecture used for these tests is described in detail below.

The architecture described herein is accommodated on a portable cart platform. As shown in Figure 3 (a) and (b), the imager collects mmW radiation from a gimbal-mounted Cassegrain antenna. While most of the components onboard the carts are the same, some are different. For the 35 GHz imager cart, the energy collected from the antenna is fed to several RF components, including a SPST PIN switch, an RF isolator, and a low-noise amplifier. The PIN switch creates a chop frequency to create a signal contrast for noise rejection techniques. The chop frequency is preset by a signal generator on the cart, which is fed to the PIN switch via coaxial cable. The chopped signal then passes to the RF isolator which allows the chopped signal to pass in one direction, as well as providing high isolation to reflected energy. The output signal of the isolator then travels to the LNA. The LNA amplifies the received signal for enhanced signal-to-noise ratio (SNR). Therefore, the noise of all the subsequent stages is reduced by the LNA gain. The aforementioned process allows the LNA to amplify the signal while adding as little noise as possible. An electro-optic modulator is the foundation piece to the imager, since it allows the incoming mmW signal to be converted to an optical signal. For this particular imager, a 40 GHz single arm phase modulator is used.
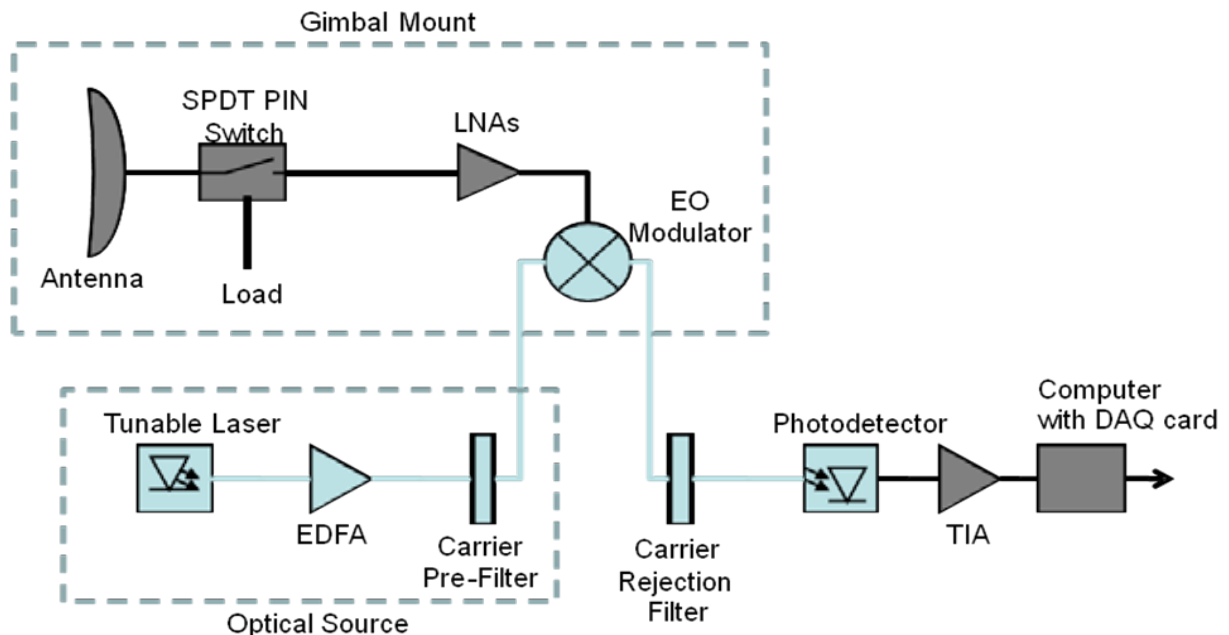

Figure 4. Schematic diagram of detector layout used for the 94 GHz scanning cart.

7

For the 94 GHz imager cart, the mmW radiation is again collected by the Cassegrain is fed to several RF components. But this setup uses a single-pole, double-throw (SPDT) PIN switch with a load, and two cascaded LNAs that have an approximate total gain of 36 dB. The SPDT PIN switch (as with the SPST switch) creates a chop frequency to create a signal contrast, and this chop frequency is also preset by a waveform generator onboard the cart, which is fed to the SPDT PIN switch via coaxial cable. The output signal of the SPDT PIN switch then travels to the two cascaded LNAs aforementioned. This particular imager employs the custom-built modulator described later in this report.

The continuous light source for the modulator on both systems is provided by a tunable laser, centered at 1546.6 nm wavelength. The tunable laser is co-pumped via an Erbium-doped fiber amplifier (EDFA). Previous work on the 35 GHz imager employed the use of a distributed feedback (DFB) laser source as the continuous light source. However, the tunable source is used now due to the fact that a tunable source is more wavelength stable. The tunable source used in both configurations is an Optilab model OTWL-C-R. Figure 4 displays a schematic diagram of the detector used for both imaging systems.
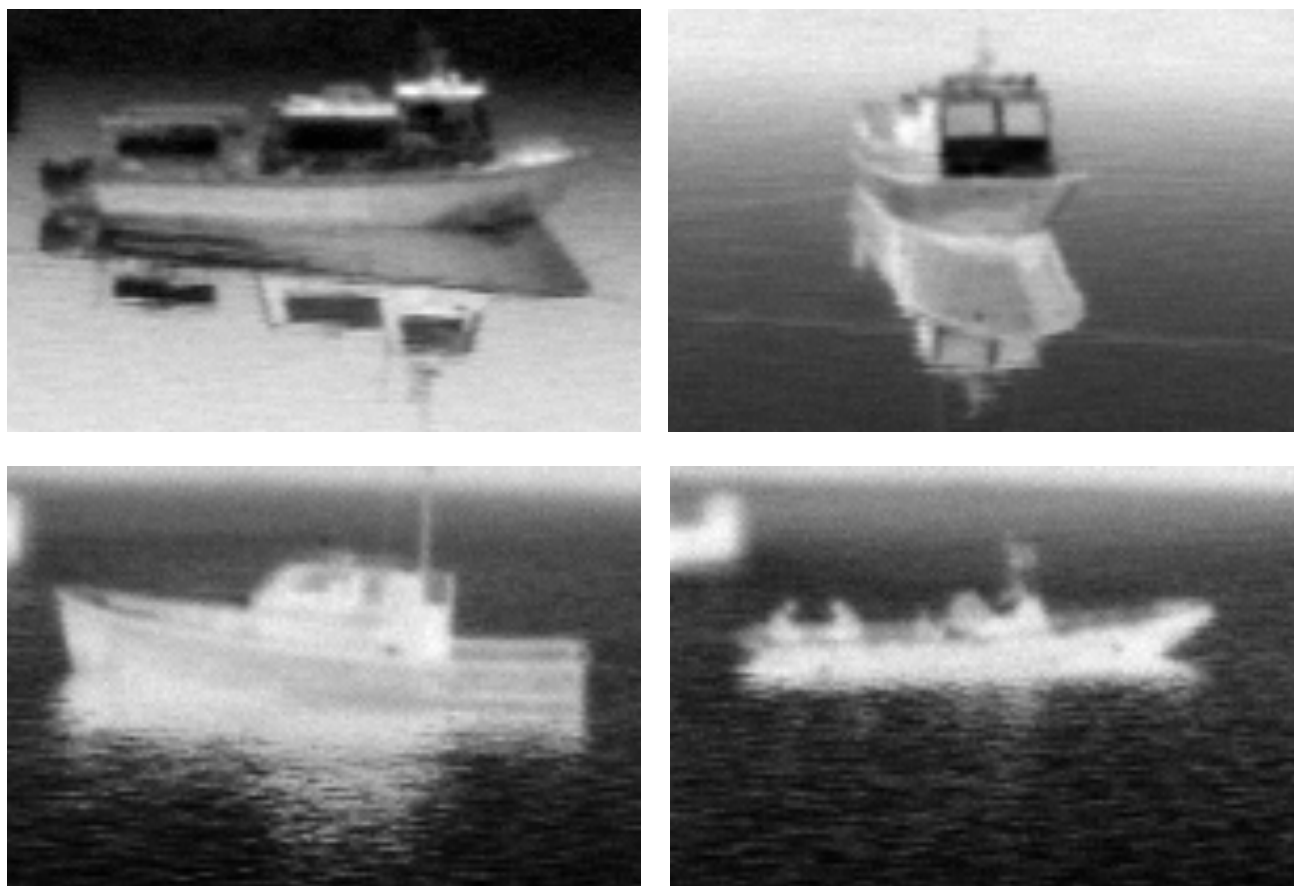

Figure 5. Sample imagery from passive millimeter-wave perception study of small watercraft.

These imaging carts have been used to produce some of the first ever data on phenomenology and perception studies in this wavelength range as shown in Figures 5 and 6. Figure 5 shows images of small watercraft taken for a study of human-factors for boat

identification in passive mmW imagery and was the first study of its kind. Figure 6 shows images taken to characterize the temperature contrast of common landing zone obstacles in a brownout environment for passive mmW imagery and has allowed the characterization of contrast requirements for passive mmW imagers for rotorcraft pilotage in degraded visual environments. The modulator packaging technique developed under this program were key to the successful realization of these studies.
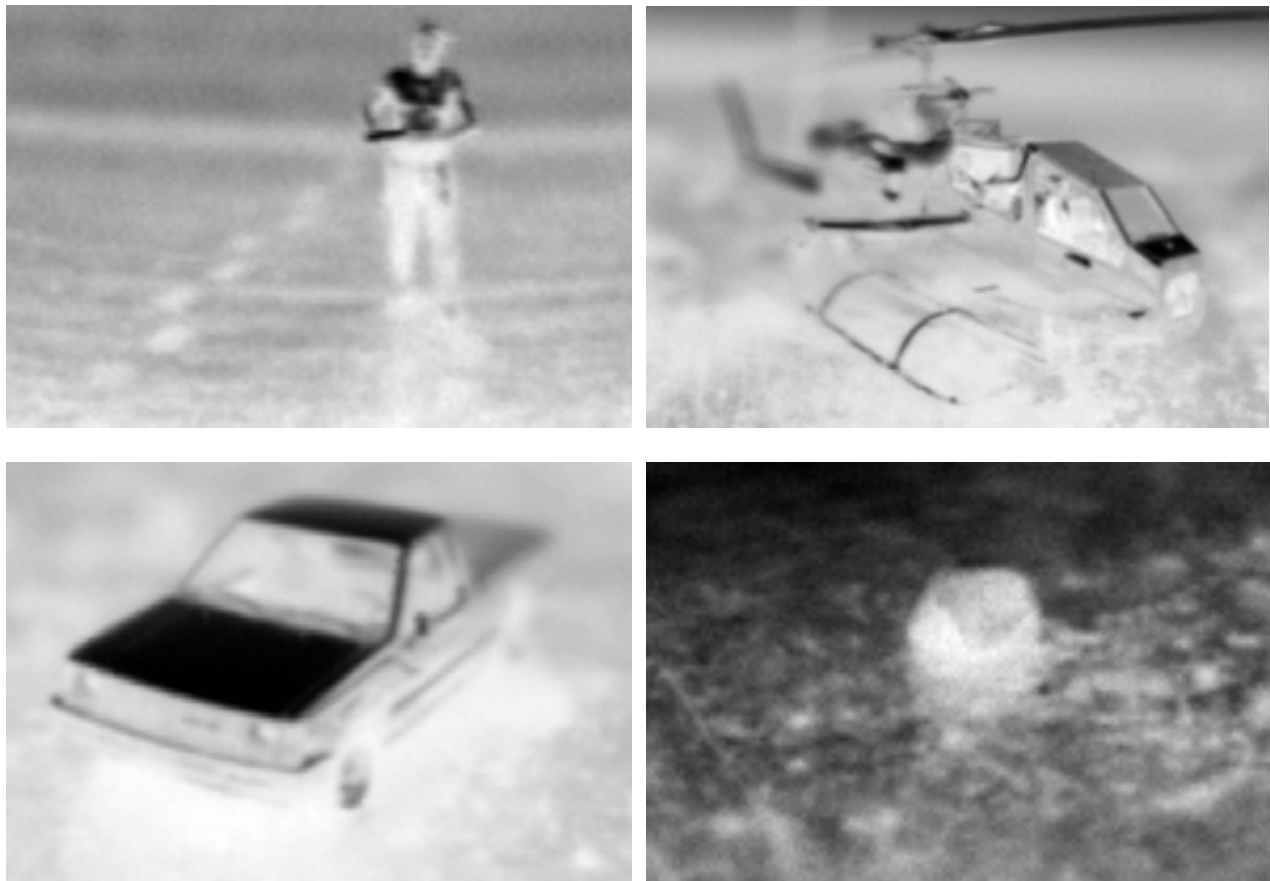

Figure 6. Sample imagery from phenomenology study of rotorcraft landing zone obstacle signatures in passive mmW imagery showing person, helicopter, truck, and boulder, respectively.

TECHNICAL PROGRESS

The primary goal of this program was to develop the required componentry to enable the creation of a W-band, optically-enabled distributed aperture imager. These efforts were in three major component areas: the development of 2-D optical component arrays mapped to the antenna array geometry, the creation of physically large, narrowband optical filters for carrier rejection, and the fabrication and packaging of optical phase

modulators with operational frequencies up to 110 GHz. In this section, we detail the progress made in each of these areas under this effort.

DEVELOPMENT AND OPTIMIZATION OF 2-D ARRAYS

BACKGROUND

For distributed aperture imagers, the quality of the processed image is highly dependent on the format of the sampling antenna array. Such imagers rely on a uniform distribution of "baselines", or the relative spacings of each element of the array to one another. This distribution of baselines is commonly referred to as the u-v coverage of the array. In general, a uniform u-v coverage is desirable for good imaging performance for an image reconstructed from a distributed array. Figure 7 shows a "Y"-array and its relative coverage in the u-v plane. Such arrays provide relatively uniformly distributed u-v coverage and are widely utilized in astronomical applications, where rotation of the array relative to the object to be imaged can be used to further fill in the u-v plane. However, for snapshot imagers such as the mmW imager in development, such rotation is not an option, and the regularity of the Y-array results in undesirable grating lobes of the PSF as shown in Figure 8. The grating lobes would ultimately lead to the creation of undesired clutter and blurring in the captured images. To avoid this effect, other configurations of antenna arrays with better sampling functions can be utilized, such as those proposed by Kogan et al[1]. shown schematically in Figure 9.
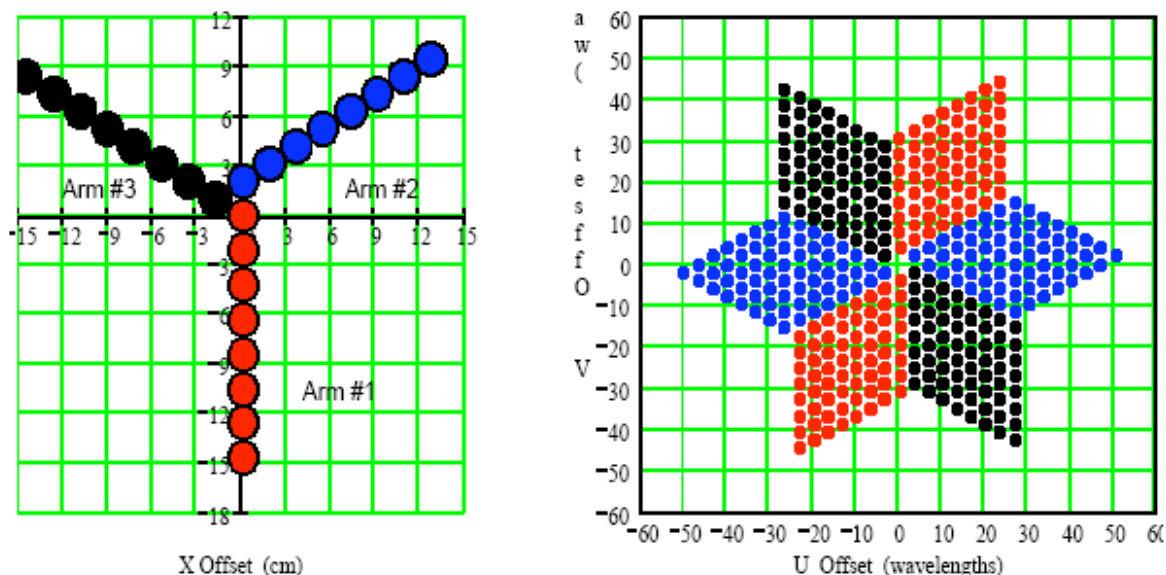

Figure 7. Typical Y-array configuration shown with relative antenna positions (left) and corresponding coverage of u-v plane (right).

---

[1] 7.Kogan, L. Optimization of an Array Configuration Minimizing Side Lobes. 1997 MMA Memo #171
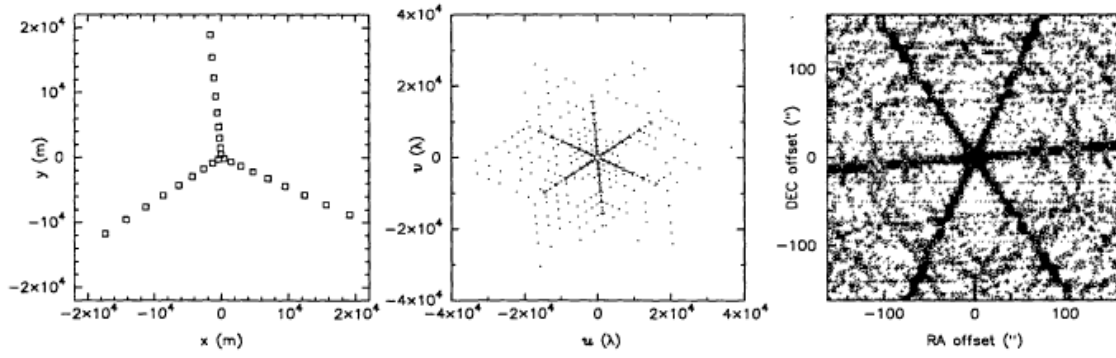
10

Figure 8. Y-array configuration used in VLA radio telescope (left), its u–v coverage without earth rotation everaging (center), and the corresponding point spread function of the array (right) showing significant sidelobe response of Y-array.
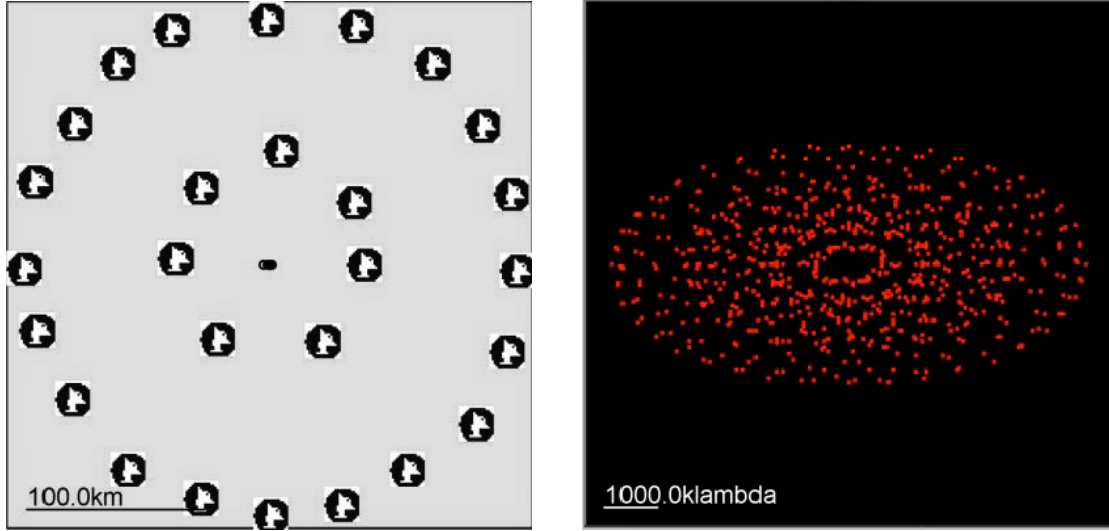

Figure 9. A Kogan array layout (left) and its UV coverage (right).

While such arrays provide a convenient mechanism for improving the quality of the reconstructed image, they present some significant engineering challenges as well. The optically based image reconstruction requires that the position of the fiber arrays directly map in a scaled fashion to the position of the mmW antennas (otherwise known as homothetic mapping). This means that the optical fibers outputs must be precisely positioned to match that of the antenna array, thereby necessitating the ability to precisely and arbitrarily place fibers in an array that matches the optimal antenna array. Further complicating matters is the requirement that the optical fibers all launch a common optical polarization, necessitating the use of polarization maintaining fibers aligned to a common launch axis.

Along with the development of fiber arrays to match 2-dimensional antenna configurations comes the need to develop collimating lenses to match. Each fiber output must be immediately coupled to a collimating lens at its termination in the optical processor to enable the phase control and carrier rejection techniques to be implemented. This means that arbitrary fiber arrays

11

must be matched to lens arrays of the same proportions. For stacked fiber array geometries, lens arrays are commercially available on pitches commensurate with the fiber diameter. However, for template based fiber geometries it may be necessary to develop lens arrays homothetically mapped to the antenna geometry as well.
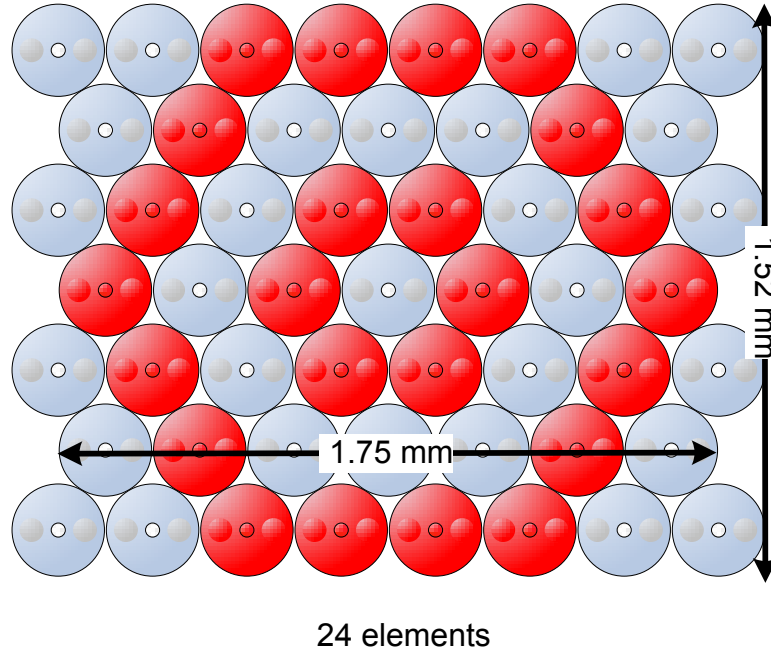

24 elements

Figure 10. Realization of a Kogan-type fiber array using close-packed optical fibers.

Finally, in order to effectively perform the optical phase compensations necessary in the desired array, the detector array, which performs the optical phase detection, would have to be engineered to match the fiber array geometry as well. This may be accomplished in one of three ways: namely, direct fabrication of detector arrays that match the fiber array geometry using semiconductor processing, pick-and-place techniques to heterogeneously fabricate detectors arrays of the appropriate geometry, or the use of commercial, high-speed IR camera's with subsequent image processing to generate phase control signals. Each of these techniques will be investigated under the auspices of this program and candidate technology will be selected and developed. Factors that will be taken into consideration are ease of fabrication, economy-of-scale, and achievable phase control bandwidth.

Under this effort, we have investigated improvements that can be achieved with the available fixed pitch arrays as well as developed preliminary processes for fabricating arbitrary arrays. Progress in these areas is presented in the following sections.

OPTIMIZATION OF FIXED PITCH ARRAYS

The optically based image reconstruction requires that the position of the fiber arrays directly map in a scaled fashion to the position of the mmW antennas (otherwise known as homothetic mapping). This means that the optical fibers outputs must be precisely positioned to match that of the antenna array, thereby necessitating the ability to precisely and arbitrarily place fibers in an array that matches the optimal antenna array. Further complicating matters is the requirement

that the optical fibers all launch a common optical polarization, necessitating the use of polarization maintaining fibers aligned to a common launch axis. To ease the fabrication of the fiber optic array a hexagonally packed array with a 250 μm pitch was used. This also enabled the use of commercially available lens arrays (Figure 11). A hexagonally packed fixture that mapped the hexagonally packed fiber array and an assembly that included the horn antenna, waveguide to coax converter and electro-optic modulator was created that enabled the reconfiguration of the RF receivers in the array. Pictures of the RF assembly and hexagonal array holder are shown in Figure 12.
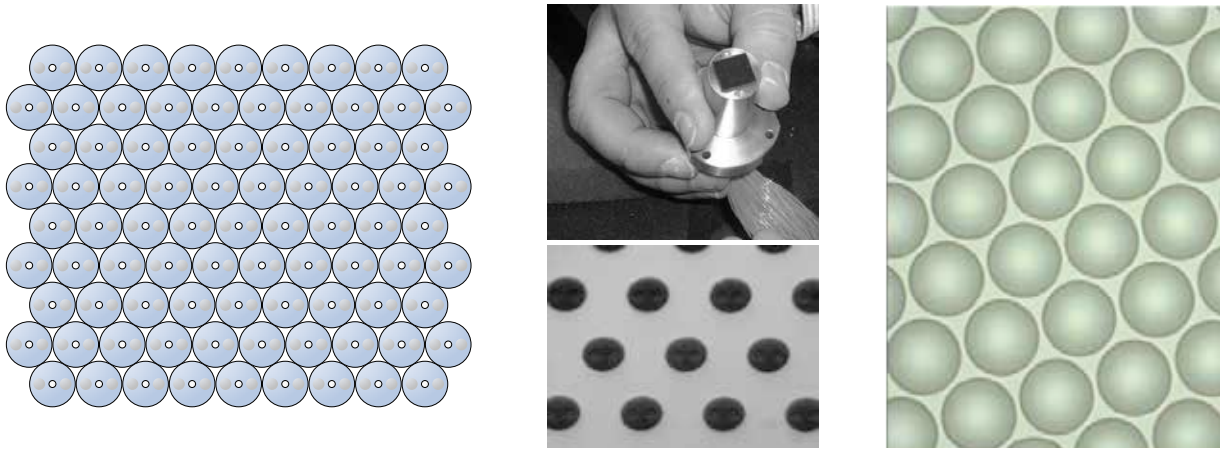
Figure 11. Schematic of 85 element, hexagonally packed, 250 μm pitch, polarization maintaining (PM) fiber array (left), photograph of the overall assembly (center top), the fiber end face showing the alignment of the polarization inducing stress rods (center bottom), and picture of commercially available lens array (right).
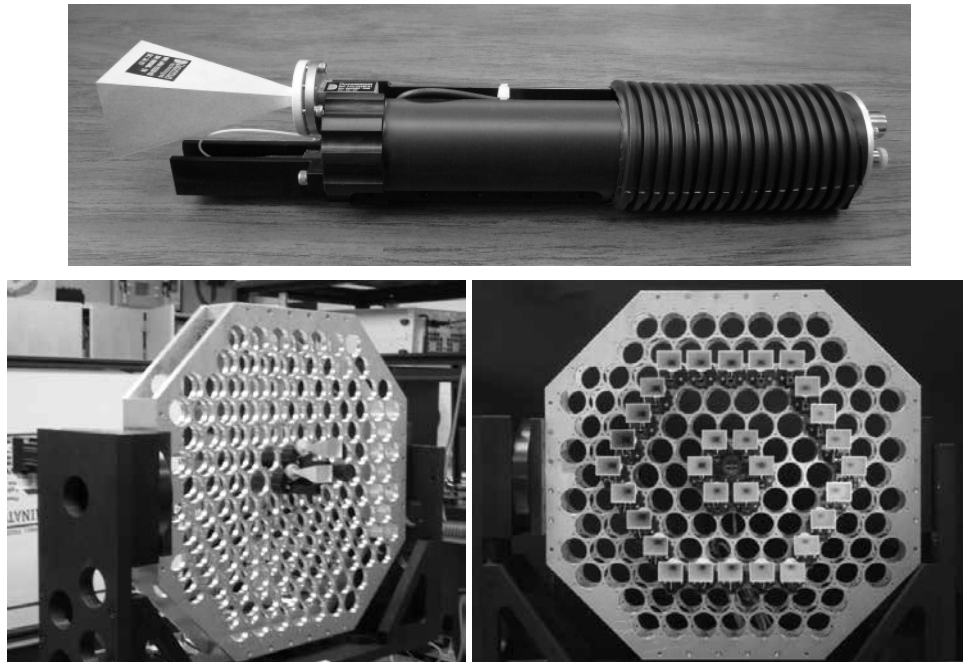

Figure 12. Photograph of a single millimeter wave detector assembly that houses the antenna, waveguide to coax converter, and electro-optic modulator (top), and photographs of the hexagonally packed receiver holder allowing for reconfigurable arrangements of detectors (bottom left and right). The bottom right photo shows a 30 element, dual ring configuration used as an initial baseline design.

Since the fiber spacing in the first imager prototype is limited to this fixed pitch array, efforts were made to optimize the point spread function that could be yielded on this fixed pitch. Using a genetic algorithm for array optimization, the optimal positioning in the fixed array was located. The merit function for this optimization simulation was based on analysis of three factors of the simulated point spread function (PSF) of the array. The factors were: the width of the main lobe, the maximum value of any grating lobes, and the total energy outside of the main lobe. The width of the main lobe was quantified by finding the maximum value of the simulated PSF around a perimeter corresponding with the half maximum point of a fully populated array. This main lobe width corresponds with the achievable resolution of the imager. The other two terms of the merit function determine the amount of background clutter generated by the sparse population of the array.

The results of this optimization are shown in Figure 13. As can be seen in the figure the resultant PSF of the optimized array yielded a significant improvement in the background clutter over the baseline array without a significant reduction in effective resolution. The optimized array demonstrates performance approaching that of the fully populated array with a 65% reduction in the number of sensor elements.

To further analyze the effect of non-optimal PSF on the imaging quality of the potential array configurations, a simulated image was generated of a sample resolution target as shown in Figure 14. From these images, the benefit of the optimized array over the baseline is more apparent.
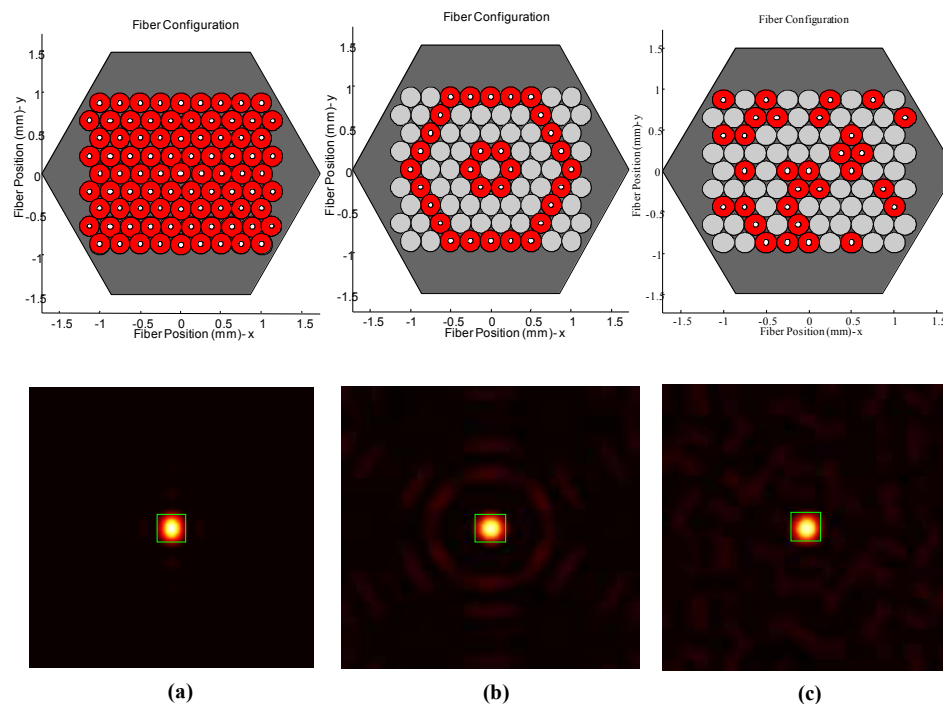

Figure 13. Simulation results for (a) fully populated array, (b) baseline hexagonal array, and (c) optimized array. The fiber positions (top) and the corresponding simulated PSF intensity plots (bottom) are shown.
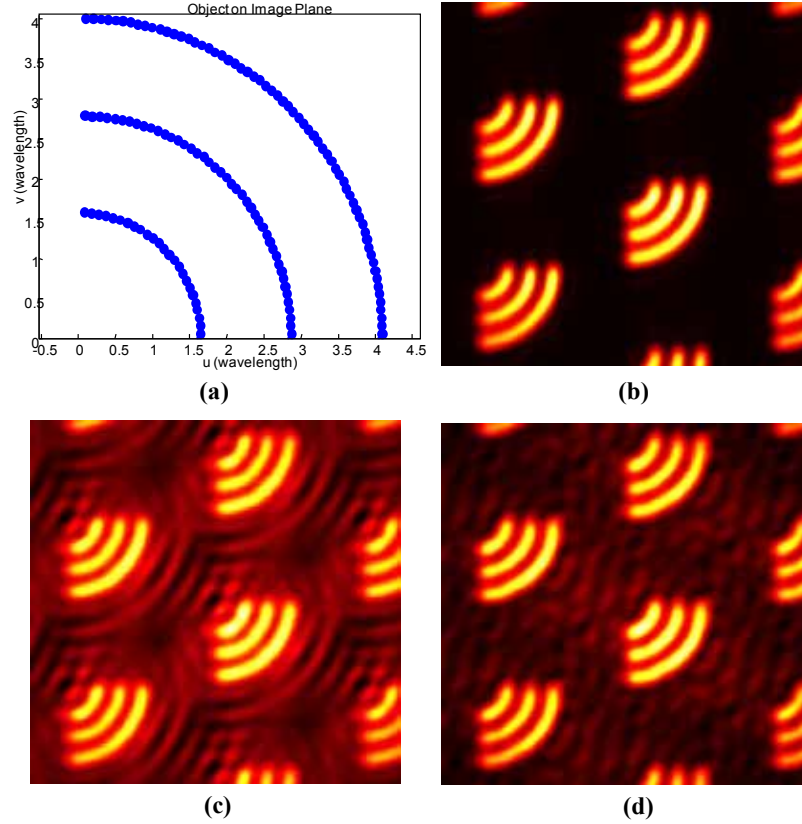
Figure 14. Simulation imagery of concentric quarter circles as shown in (a) for (b) fully populated array, (c) baseline hexagonal array, and (d) optimized array. Aliasing in image is a result of minimum fiber spacing that limits viable field of view.

ARBITRARY ARRAY DEVELOPMENT- FIBER ARRAY

The typical method to produce 2-D fiber arrays is to produce micromachined silicon mechanical templates to hold the fibers in place with a precision approaching one micron. Thus, the ability to produce the desired arbitrary fiber array geometries is mainly governed by the ability to produce these silicon templates. These templates are formed by using an anisotropic deep etching processes to form lithographically defined holes in a silicon wafer. In order to populate these holes with fiber, the formed holes must have a slight taper.

Given these findings, we adjusted the process parameters for the Bosch etch process, which is typically used for high aspect ratio, anisotropic etching of silicon. This process combined a repetitive cycling of anisotropic etch, isotropic etch, and sidewall passivation in a inductively coupled reactive ion etcher to produce extremely anisotropic etches that are typically optimized for vertical sidewalls. To attempt to produce the desired slight taper of the sidewalls, the duration of the etch step was decreased. This etch resulted in the 125 µm vias as shown in figure 15. However, we found that significant sidewall roughening resulted as well as a greatly reduced etch rate. The roughening is readily apparent in the via sidewalls towards the bottom of the via. As a result, we sought an alternative means to produce the appropriate sidewall angle while maintaining a high etch rate. We found such a technique in the literature to achieve this, called

tapered deep reactive ion etching (TDRIE). This process is illustrated schematically in figure 16. In this technique, the Bosch process is interrupted every few cycles by a short isotropic etch, which has the effect of widening the via at the top, thus compensating for the negative sidewall angle that is typically observed for the larger via sizes.
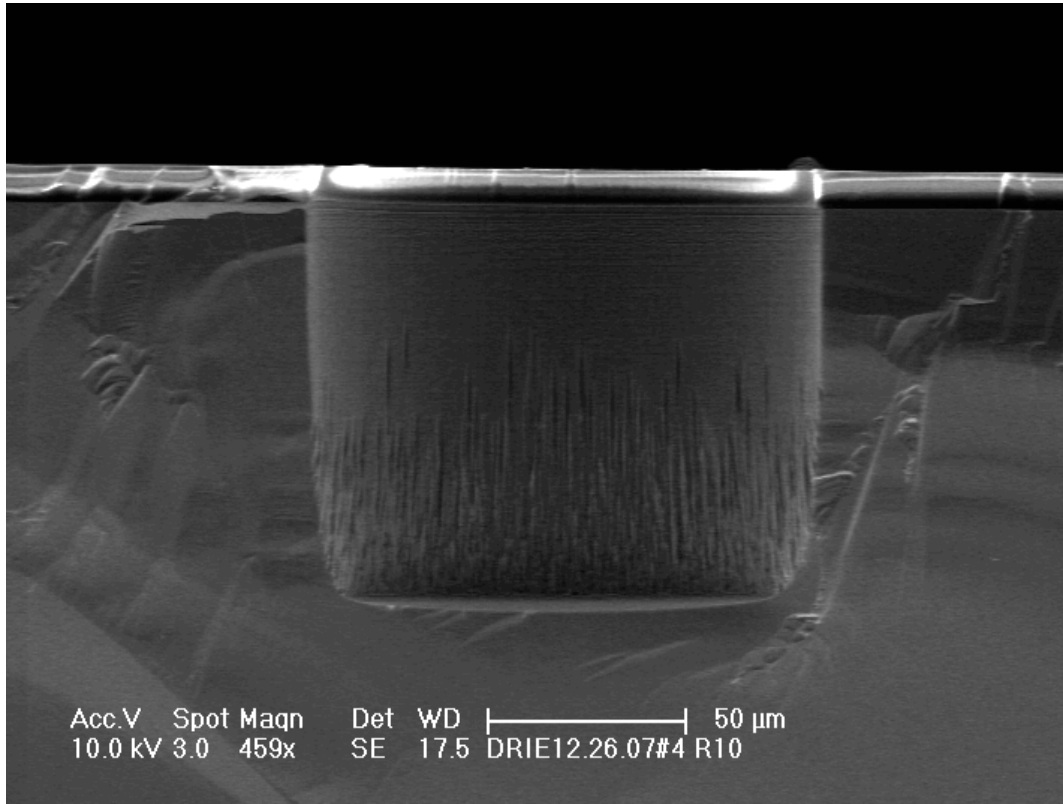

Figure 15. First observation of positive sidewall taper in a 125 μm via obtained by adjustment of the etch cycle duration.

We investigated the effect of the isotropic etch cycle duration in the TDRIE process on the sidewall angle of the via; these results are shown in figure 17. Without an isotropic etch cycle, a negative sidewall angle is observed. For 5 second isotropic etch time, near vertical sidewalls result. As the isotropic etch cycle duration is further increased, a positive sidewall angle is observed, which is favorable for the through-wafer etch for fiber insertion. Results of the application of this process are shown in figure 18. We were able to etch through the entire thickness of the wafer handle, an etch depth of approximately 400 μm, in under 80 min, for an etch rate in excess of 5 μm/min.
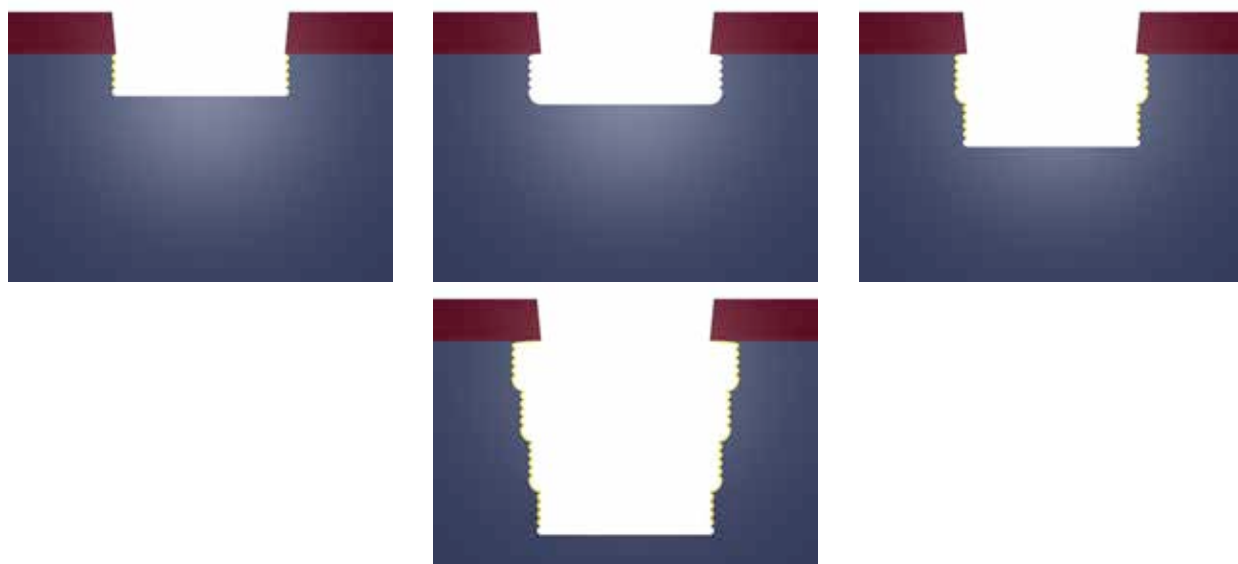
16

Figure 16. Illustration of the TDRIE process steps. The Bosch process proceeds normally for several cycles (top left). It is then interrupted by a short isotropic etch step (top right). The Bosch process is then repeated (bottom left). After many repetitions, a positive sidewall angle is observed (bottom right).
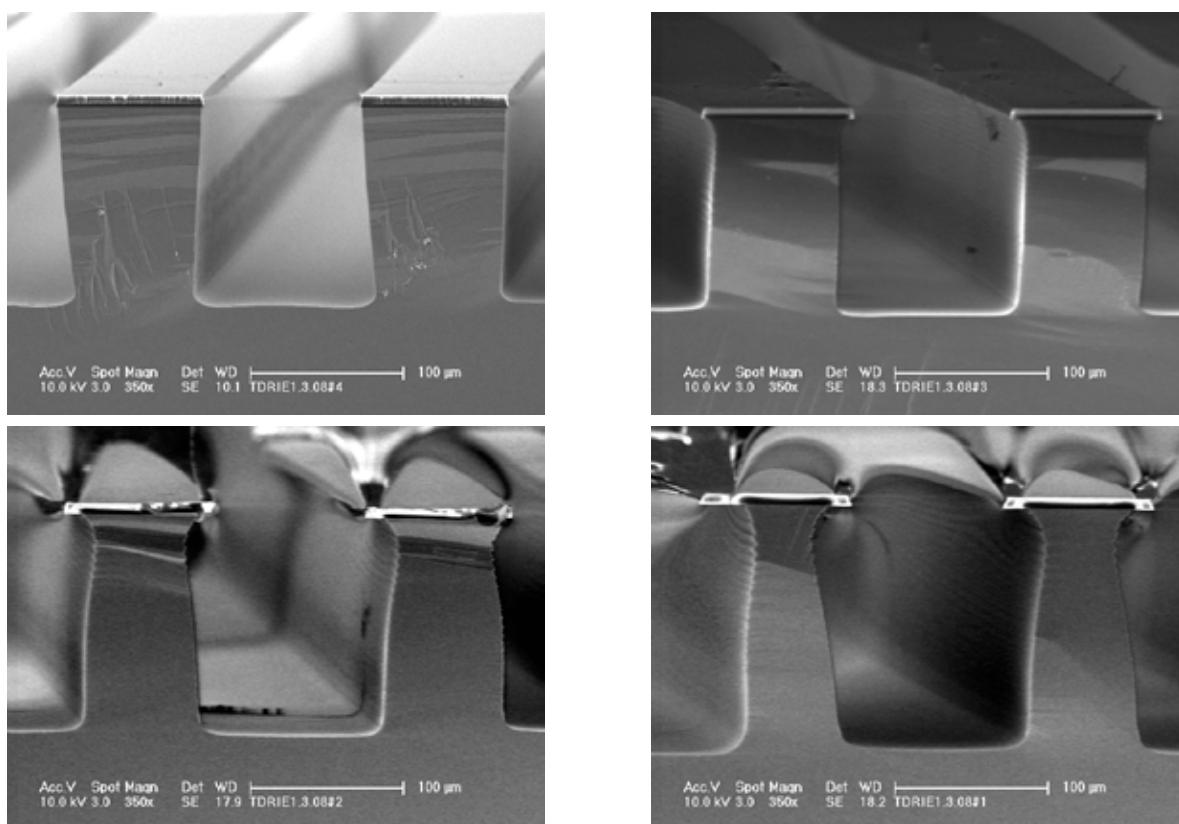

Figure 17. SEM images illustrating the effect of the isotropic etch cycle time on the trench sidewall angle for the TDRIE process. Isotropic etch cycle times are 0 seconds (top left), 5 seconds (top right), 10 seconds (bottom left), and 15 seconds (bottom right). As the etch time is increased, the sidewall angle becomes more positive.
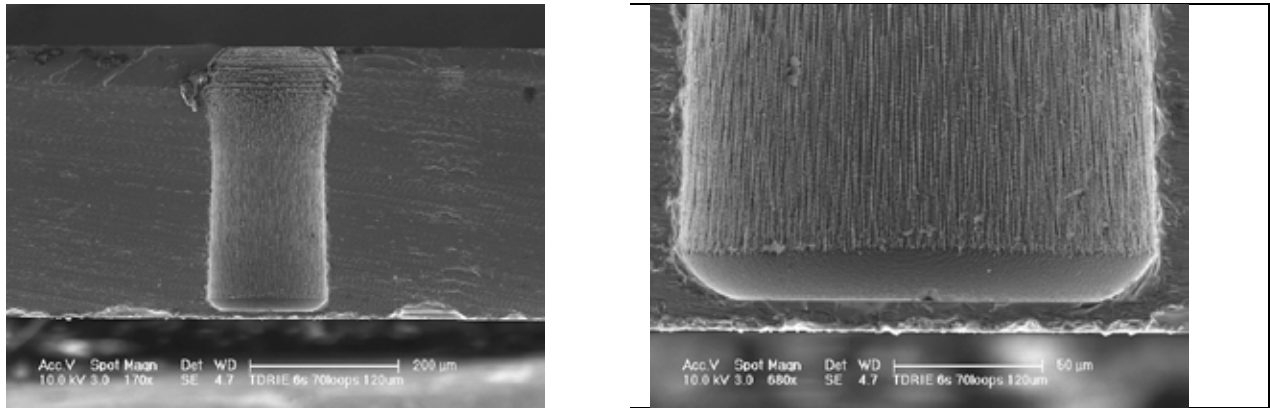
17

Figure 18. Through wafer etch results using the TDRIE process. The buried oxide layer can be seen at the bottom of the via (right).

In order to validate the concept of the through-wafer etch for the optical fiber via, we prepared a sample using the TDRIE etch process developed here followed by cleaving and polishing through one such via and inserting an optical fiber, as shown in figure 19. The fiber fit into the via completely and with minimal slop. As a result of this effort, we have demonstrated the feasibility of etching through-wafer vias for optical fiber insertion. Continuing efforts will be focused on optimizing these etch profiles and developing techniques to populate the fiber arrays.
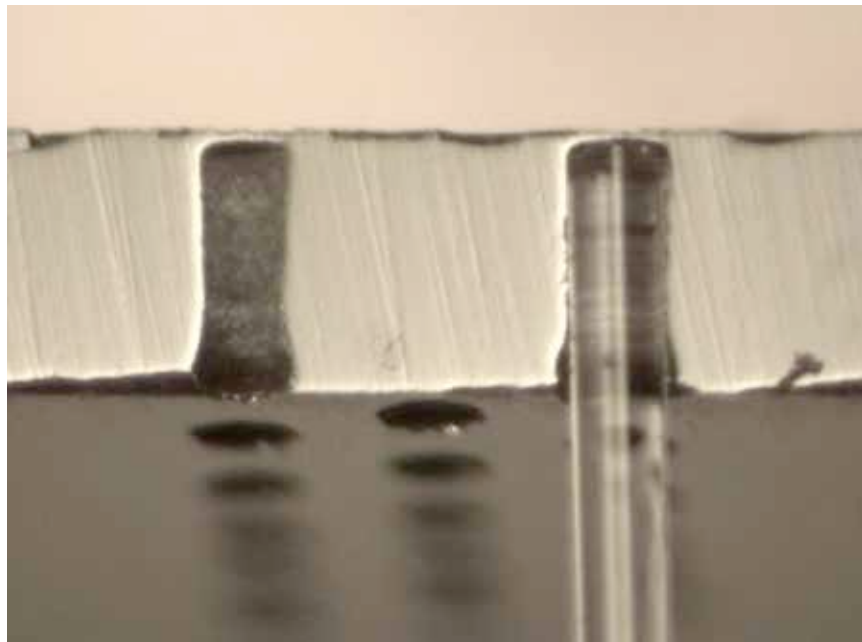

Figure 19. Through wafer etched via with optical fiber in place.

Under this effort we have developed grey-scale processes for the creation of lenslets to focus the individual fiber outputs in the array. For this effort, we have chosen to pursue Fresnel zone plates fabricated using grayscale lithography. Although these processes can be directly applied to more traditional refractive lenslets, we believe Fresnel lenses will provide the highest degree of freedom in terms of fill factor, focal length, and diffraction efficiency for this application.

Fresnel lenses are diffractive optical elements (DOEs) that can be designed by phase wrapping the refractive lens counterpart, as shown in figure 20. Most simply, a Fresnel lens takes the form of a Fresnel zone plate, which consists of only two phase levels 180º out of phase. This type of lens can be easily fabricated using standard binary photolithographic techniques. However, the zone plate has a low diffraction efficiency; that is, much of the optical energy in the focal plane falls outside the Airy disc. Although the example of figure 20 shows an optical surface quantized into only four discreet levels, use of a continuous tone grayscale mask such as HEBS glass allows for smoothly contoured surfaces that result in lenses with very high diffraction efficiency. Because these phase surfaces can be made arbitrarily, aspheric lenses with aberration correction are also feasible.
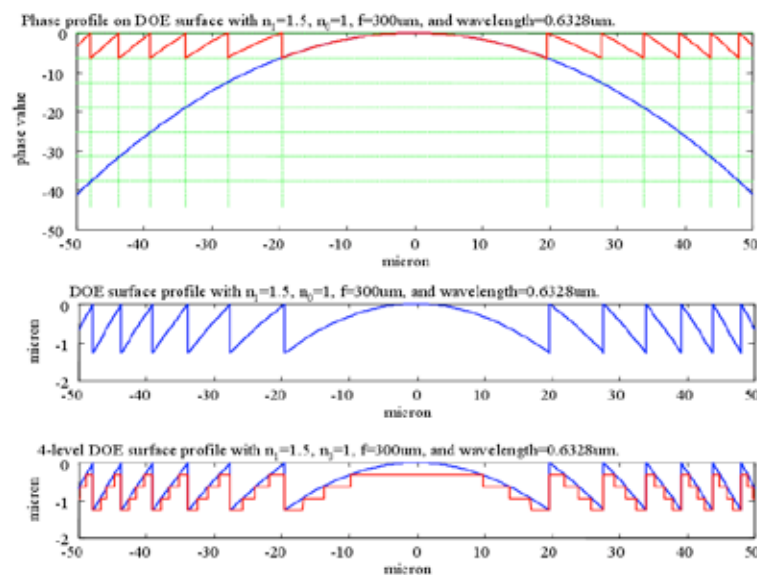

Figure 20.   Design of Fresnel lens.

As a result of the phase wrapping inherent in the Fresnel lens, these devices can be made very thin, with a relief depth on the order of the wavelength of light within the material. Consequently, they are preferred in some applications where weight and volume are critical. By virtue of the lithographic fabrication approach, they can be made in batch form in lens arrays, which results in low unit cost per lens. There are also applications where the array form of the lenses is beneficial; for example, arrays may be used to increase the effective fill factor of an FPA where there is interstitial space between the individual detectors, or they may be used in multiple aperture imaging systems. This feature is particularly useful for this application where

the ability to achieve 100% fill factor and minimize stray light is of utmost importance. Furthermore, the flexibility of the fabrication technique allows for the properties of the lenses to vary across the array. Although there are many situations where the use of Fresnel lenses may be preferred over refractive lenses, it is important to note that they suffer from severe chromatic aberrations and may be impractical for broadband applications, but are ideal for this application where the optical energy is effectively very narrow band.
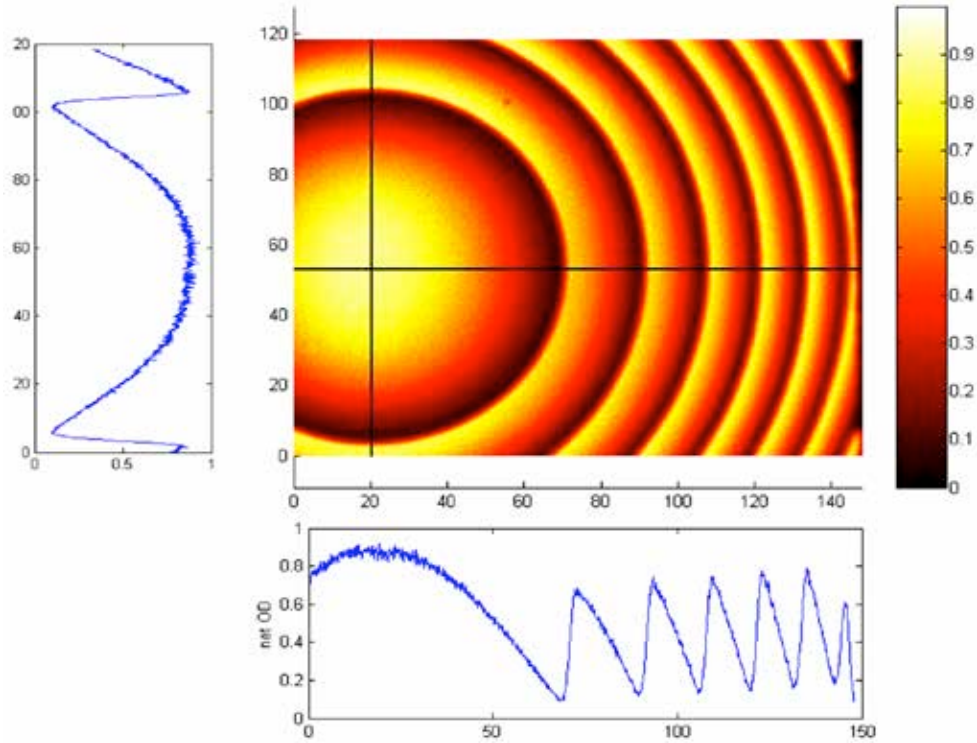

Figure 21. HEBS mask image and optical density cross-section for Fresnel lens grayscale pattern.

In order to fabricate the Fresnel lenses, we used the surface relief profile as determined in figure 20 and encoded the grayscale levels of the HEBS glass photomask based on the contrast curve of the photoresist. For some applications, AZ5214 was used as it produced a film thickness of about a micron. This results in the appropriate surface relief for many NIR applications. In other work, we used the AZ4000 series photoresists which result in thicker films. This was done in some applications where the Fresnel lens was designed with higher order phase wrapping. For very low f/# lenses, the higher order wrapping increases the width of the Fresnel zones and therefore eases fabrication.

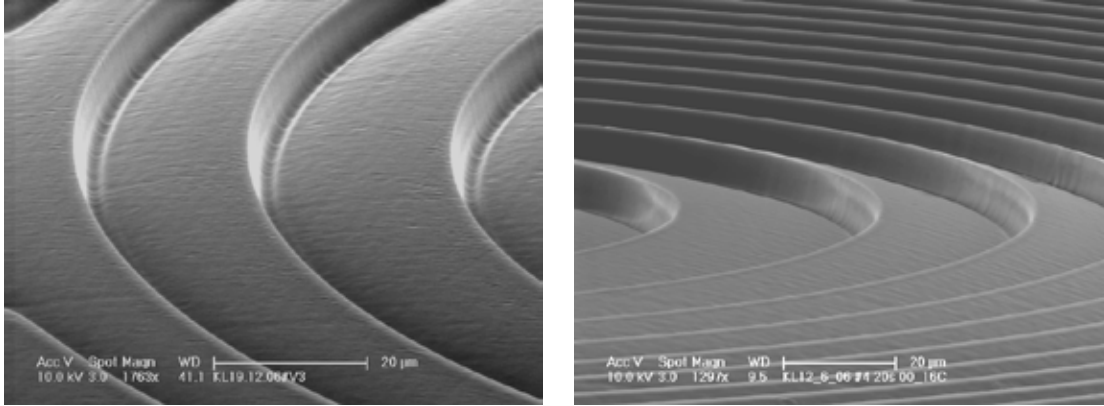**Figure 22.** Close-up SEM images of Fresnel lenses in photoresist.

Once the appropriate grayscale values for the photomask were determined, the pattern was fractured into a set of concentric single pixel circles each with the appropriate electron dose according to the HEBS glass sensitivity curve. The mask was then exposed in the Raith 50 electron beam lithography tool, resulting in patterns such as those shown in figure 21. This figure shows some variation in the peak optical density across the Fresnel zones of the lens; later work using proximity effect correction improved upon these results. Close-up images of Fresnel lenses fabricated with a photomask such as this are illustrated in figure 22. From these images, the smooth surface contour within Fresnel zones is apparent, along with the discontinuities between Fresnel zones due to phase wrapping.
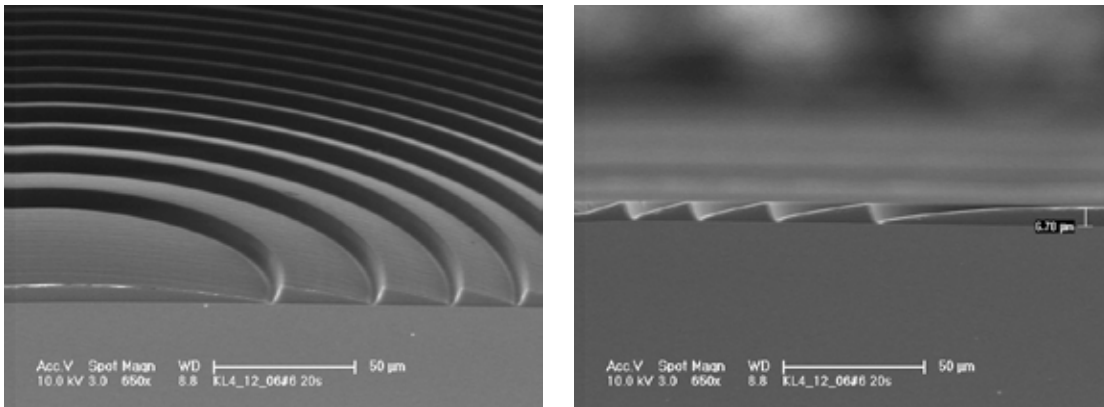

Figure 23. Cross-sectional SEM images of Fresnel lenses in photoresist.

In order to further examine the photolithographic results of the Fresnel lens fabrication, samples were prepared for SEM imaging by cleaving the wafers through the Fresnel lens and then viewed in cross-section. Images collected in this fashion are shown in figures 23 and 24. Comparison of the images of figure 24, where Fresnel zones near the center of the lens are compared to those near the edge of the lens, indicates the difficulty in realizing the very narrow Fresnel zones that can occur near the edge of the lens for low f/# lenses. It is apparent that the modulation depth of the photoresist is reduced for the higher spatial frequency patterns. Also apparent is the non-vertical discontinuities at the Fresnel zone boundaries which represents the resolution limitations of this fabrication method.
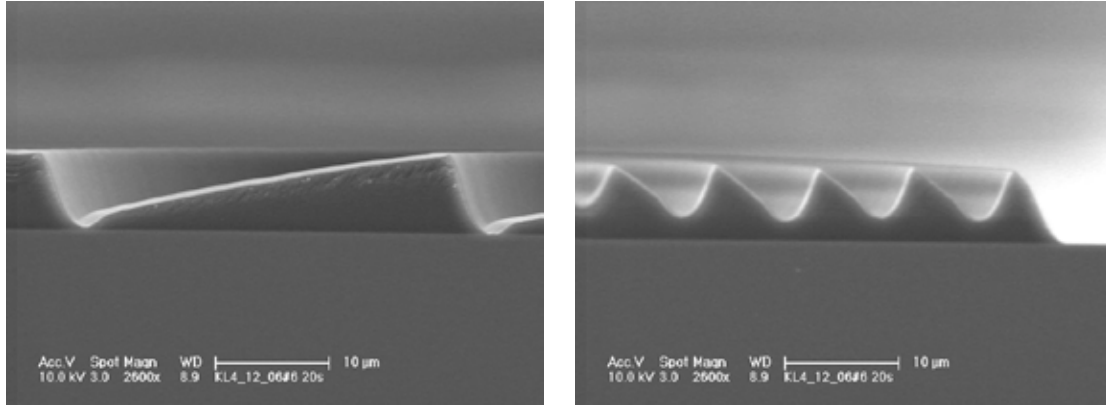
Figure 24. Comparison of Fresnel zones near the center of then lens (left) and at the edge of the lens (right) for a low f/# lens.

The atomic force microscope (AFM) is another tool useful for inspection of the fabricated Fresnel lenses. We used special high-aspect ratio AFM probe tips to take measurements of the lens surface relief, as shown in figures 25 and 26. These exceptional measurements indicate the quality of the surface smoothness and uniformity of the modulation depth of the Fresnel zones. The latter represents an improvement over the early mask writing results of figure 21. The Fresnel lenses presented here were designed with multiple order phase wrapping and resulted in a surface relief of approximately 4.4 μm at the lens center and a sidewall angle at the Fresnel zone boundaries of approximately 50º. A measurement taken from the edge of the Fresnel lens is shown in figure 26. This particular image appears very similar to a curvilinear blazed diffraction grating; the fabrication method for the Fresnel lens is directly applicable to the realization of this class of devices as well.
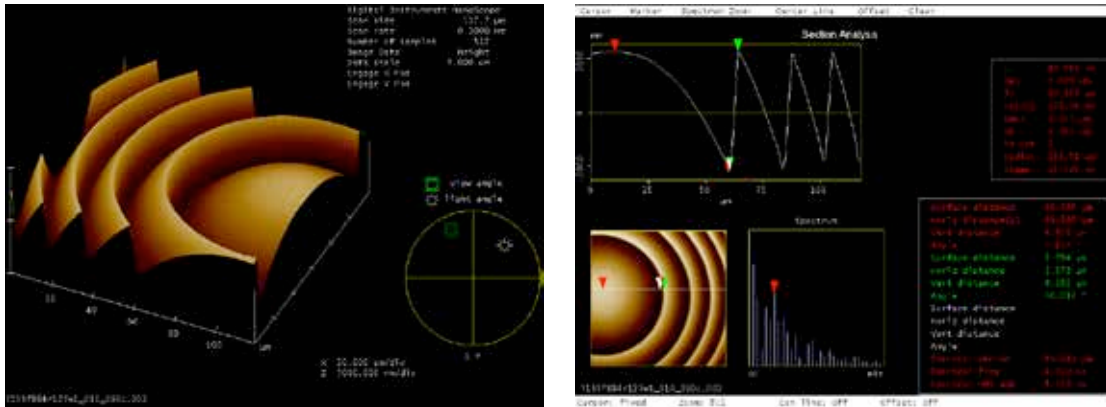

Figure 25. AFM profilometry near the center of a Fresnel lens.

A third method for assessing fabrication results for the Fresnel lenses is white light interferometry. We used a Wyko rollscope from Veeco to take such measurements, as shown in figure 27. This method has the advantage of being much faster than the AFM since it captures the entire surface profile in a single measurement, whereas the latter is by nature a serial scanning technique. On the other hand, it is often necessary to coat the samples with a thin layer of chrome or other metal to improve the reflectivity of the samples and achieve good

22

measurements. Such coatings are often necessary for SEM measurements as well, to mitigate charging effects that result in distorted imagery. An additional drawback to using the Wyko is that it can be impossible to measure large surface angles because they may not be collected by the limited numerical aperture of the used objective.
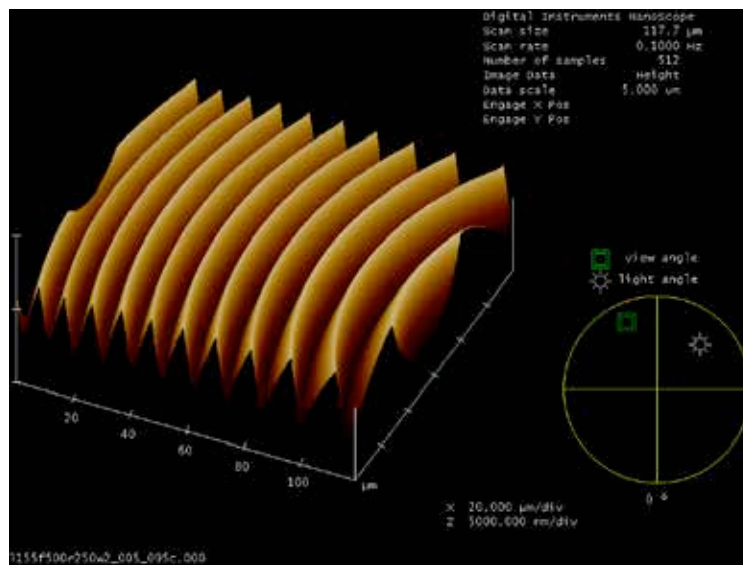

Figure 26. AFM profilometry near the edge of a Fresnel lens.

After the Fresnel lenses have been realized in photoresist by the grayscale lithography process, often they will be transferred into the underlying substrate material by a plasma etch process. An SEM image of a lens transferred into quartz by this method is shown in figure 28. Close examination of this image reveals that some grass or nodules are present on the surface of the lens, most likely due to micro-masking. Also there appears to be some texture in the surface of the lens. We believe this to be present in the photomask itself due to grid-snapping or some other issue with the pattern generator during the exposure of the HEBS glass in the Raith 50 exposure tool. However, these issues appear to be minor and would not be expected to seriously impact the optical performance of these devices.
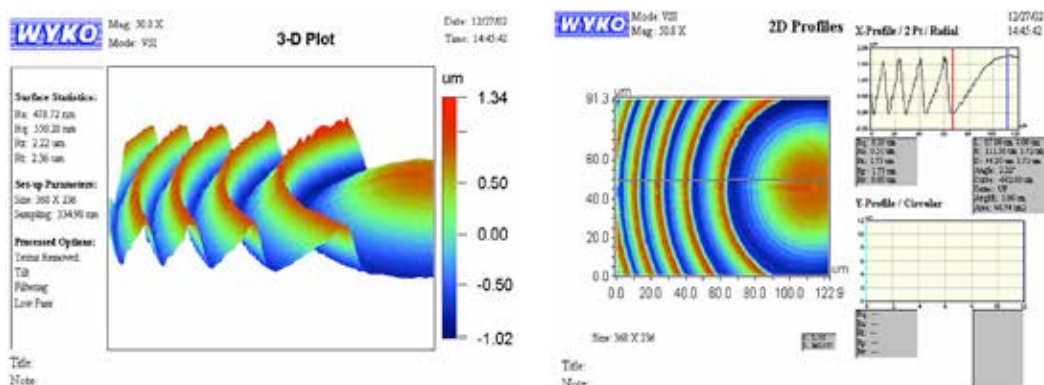

Figure 27. White light profilometry for Fresnel lens.

The devices shown herein can be lithographically defined on an arbitrary pitch and with a 100% effective fill factor. Such devices when optimized will enable the use of arbitrary fiber arrays for the desired millimeter-wave imagers and increase the available field-of-view accessible using this imaging architecture.
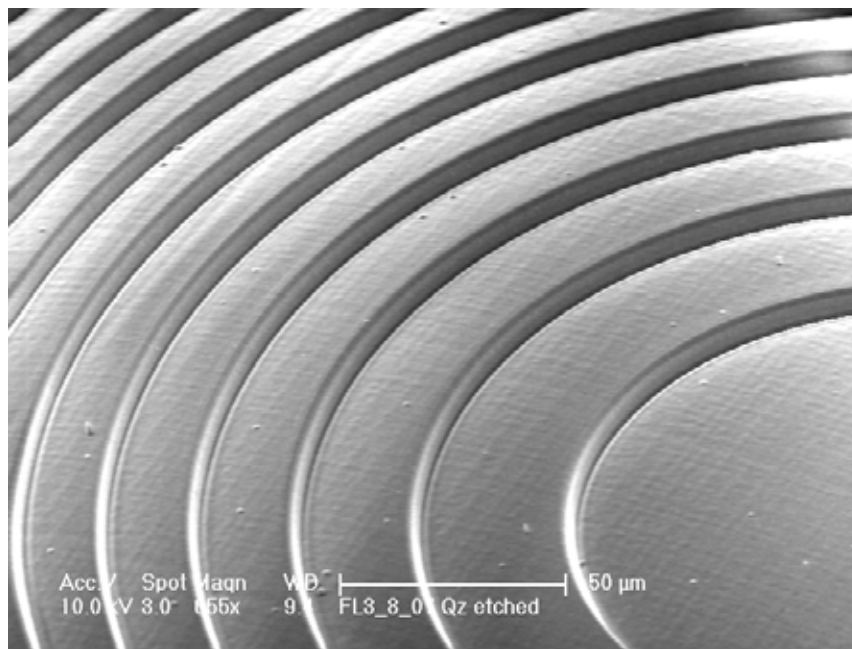

Figure 28. Fresnel lens etched in quartz.

ARBITRARY ARRAY DEVELOPMENT- DETECTOR ARRAY

In order to produce arbitrary array layouts, a customized photodetector array must be built to sample the optical phases of each beam in real time. Since the desired phase control loop must be able to compensate for vibrations of the optical fiber, the photodetector array must be capable of operating at update rates greater than 20 kHz. This fact precludes the use of standard InGaAs camera to perform phase control as such camera cannot sample multiple spots in the array at these rates. This bandwidth limit is mostly imposed by the multiplexing of the readout integrated circuitry (ROIC) when accessing the many pixels of the array. Under this effort, we analyzed many possible techniques for yielding the required detector array with sufficient bandwidth. Out initial intention was to have a custom detector array fabricated from scratch from an epitaxial grown InGaAs wafer. However, on further review, it was concluded that standard InGaAs imaging arrays could be utilized provided they were decoupled from the ROIC's. To this end, several InGaAs arrays were purchased and evaluated for suitability for bonding to a custom fanout interposer board. These interposer boards would access pixels corresponding to the desired arbitrary layout and relay the outputs of those pixels to an off chip amplifier and signal processing board. This approach was considered low enough risk that efforts were concentrated on other higher risk development areas with equal importance for the duration of this development effort.

OPTICAL FILTER DEVELOPMENT

The optical filters that are used to perform carrier rejection are a key element of the performance of the system. Currently, commercial optical add/drop multiplexer filters based on thin film coating stacks are used to achieve the desired narrow filter function. These filters were developed for the telecommunication industry to allow dense wavelength division multiplexing on fiber optic channels. As such, the active area of the available filter chips is typically on the order of one millimeter or less. In order to implement larger two-dimensional arrays using the carrier rejection technique, we anticipate that filters with uniform areas as large as 1 cm square may be necessary for many applications. Initial conversations with filter vendors have indicated that this level of uniformity may be difficult to achieve due to strain inherent in the coating process limits the uniform areas that can be achieved with current processes. Figure 29 shows a sample uniformity chart from one such filter vendor.
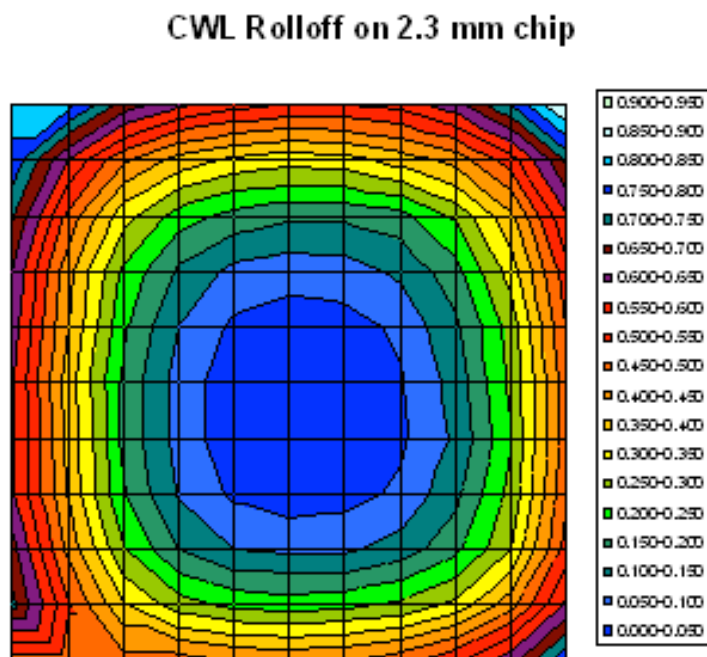

Figure 29. Filter uniformity across a 1.8 mm commercial OADM filter coating.

For the purposes of the proposed distributed aperture imager, a filter center wavelength deviation of 0.1 nm or less is desired. As is apparent in Figure 14, this limits the usable optical aperture to ~1 mm^2. Since the minimum practical fiber spacing is 250 μm, as determined by the clad fiber diameter, the existing filter technology limits the realizable array size to roughly four elements. As part of this program, we will solicit bids from the various filter vendors to perform the NRE necessary to improve the uniformity of their existing filter technology. Our target for this effort was a filter with a uniformity of ±0.05 nm across a 1 cm^2 area.

The optical up-conversion process is schematically illustrated in figure 1. A laser operates as an optical power supply producing a quasi-monochromatic output that feeds an electro-optic modulator. Millimeter wave radiation that is collected by an antenna is also fed to the modulator, where it creates upper and lower sidebands on the carrier by the non-linear behavior

of the modulator. An example of the resulting signal is shown in figure 30. The optical carrier and extraneous sidebands are then suppressed using the narrow bandpass optical filter. For a single pixel imager, the following step is conversion to DC using a photodetector. For the distributed aperture imager discussed here, optical signals from a large number of detector channels are interferometrically combined to produce a snapshot image.
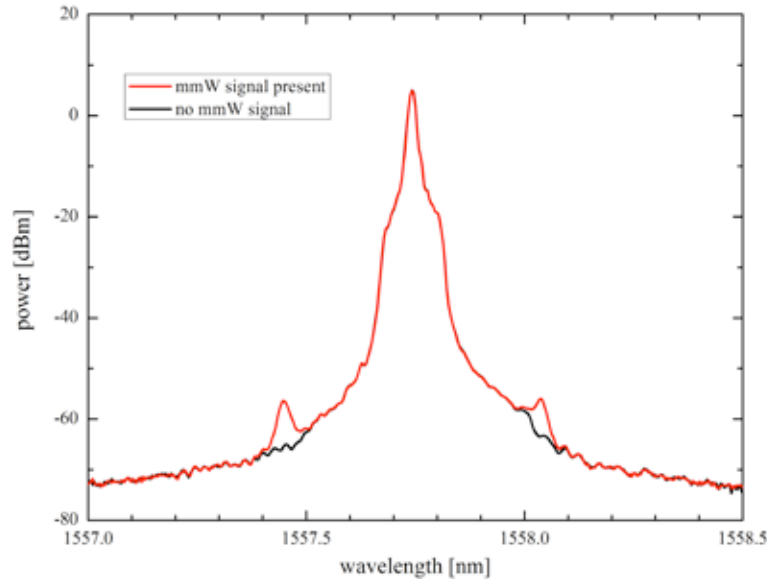

Figure 30. Signal produced at the output of the modulator where the mmW radiation has been optically up-converted to the sidebands on the optical carrier. Because of the weak passive mmW signals involved, the sidebands are much lower in power (~ -70 dBc) than the optical carrier, therefore necessitating a large amount of carrier suppression by filtering.

Since the sidebands contain much lower optical power than the carrier, approximately -70 dBc, a large amount of carrier suppression is required. To facilitate this, it is convenient for the separation between the sideband and carrier to be large, since there are limitations to the sharpness of the filter response. However, due to technological limitations on the speed of the commercially available modulators as well the fixed locations of the available low attenuation bands in the mmW spectrum, 35 GHz was chosen as the operating frequency of the present imaging system. Development of modulators for system operation at higher frequencies are underway, as described elsewhere in this report, which will ease requirements on the optical filters for achieving sufficient carrier suppression.
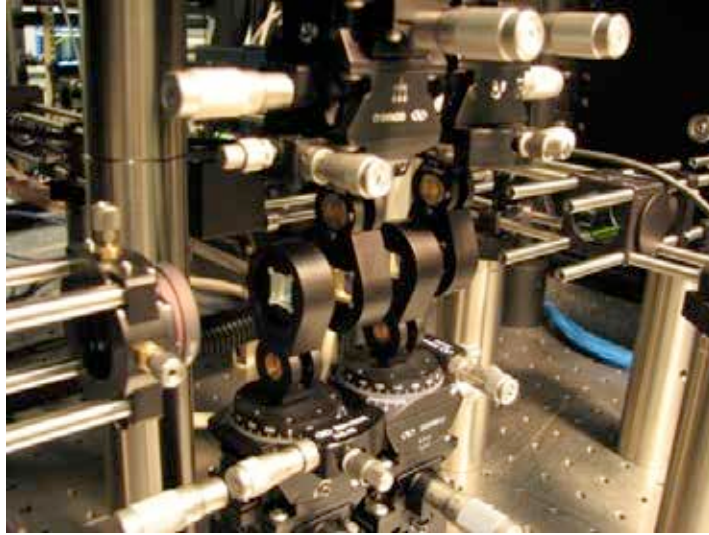
Figure 31. Four 100 GHz channel spacing OADM optical filters were required to achieve sufficient carrier rejection to achieve passive operation for the 35 GHz imaging system.

As shown in figure 31, a total of four filters were incorporated into the optical back-end of the current imaging system to achieve the required level of carrier suppression for passive imaging. Whereas a single pixel scanning imager requires only a single detector channel, the distributed aperture imager requires a number of channels which are subsequently combined to produce a two-dimensional snapshot image. These optical channels must all be filtered concurrently and preferably using the same optical filter, so that they all receive the same filtering and consequently the relative power of each channel is preserved. To elaborate on this latter point, consider a set of filters with slightly shifted center frequencies relative to one another, where each individual channel uses its own optical filter. In some instances, the shift in filter response causes the corresponding channel's signal to lie near the edge of the filter envelope, resulting in attenuation that varies from channel to channel depending on the displacement of the center frequency for each individual filter.

In order to maintain integrity of the individual channels while passing them all through the filter concurrently, two optical designs are conceivable: one where the individual channels are passed through the filter at the same angle but with spatial separation, and one where the channels are passed through at different angles but the beams all overlap at or near the filter. It has been our experience that the spatial separation approach results in a degraded filter response and lower out-of-band rejection when the array of channels is imaged onto the filter to realize this approach. On the other hand, when angular separation is used each individual beam corresponding to each of the channels is allowed to have a beam diameter approaching the clear aperture of the filter. In effect, each channel is passed through the filter as a collimated beam and therefore the sharpness of the filter response is preserved. However, because of the blue-shift in the filter response for non-normal incidence, it is desirable to keep the incidence angles near normal. This necessitates the use of a filter with large area aperture, for reasons that will be discussed in more detail later.
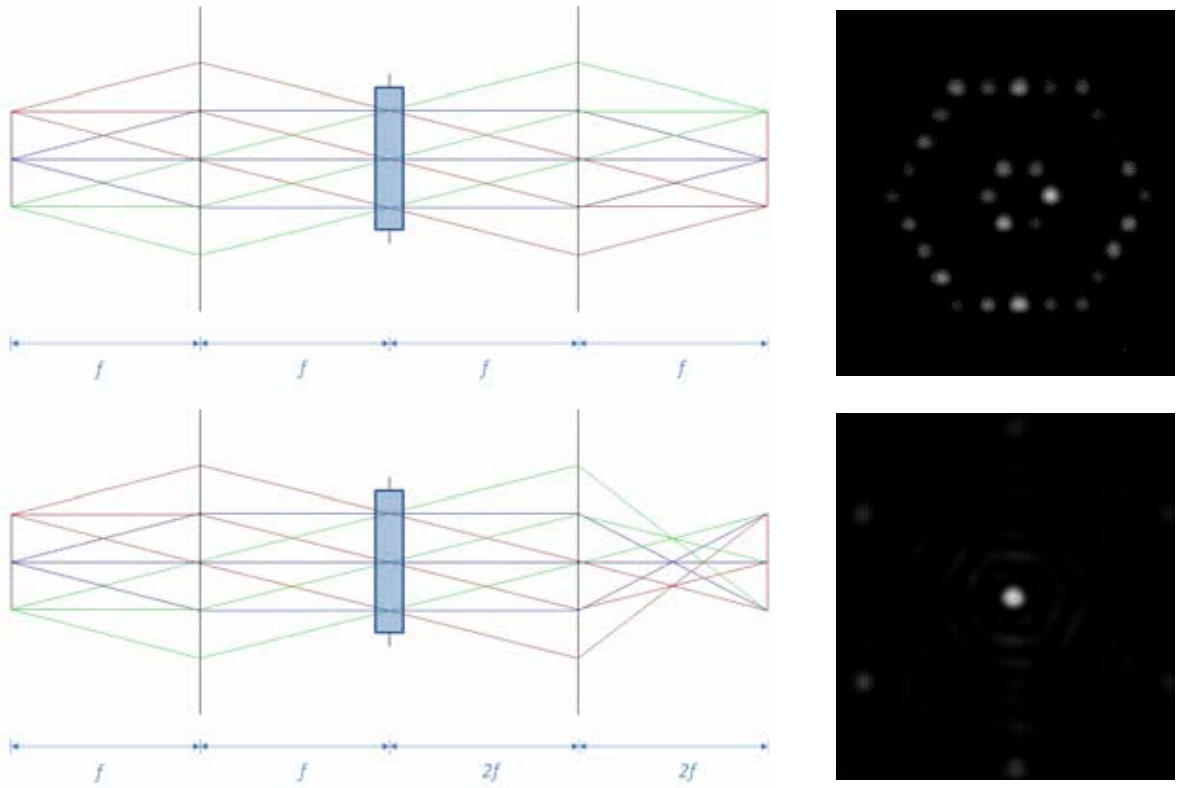
27

Figure 32. Paraxial ray-trace of the image forming optics (left) and corresponding images (right). One can switch between the two optical configurations shown by simply swapping the second lens. A 4-f configuration (top) is used to pass the optical beams through the filter and reimage the source array stripped of the optical carrier; this is useful for filter alignment adjustments and other diagnostic purposes. A 6-f configuration (bottom) is used to pass the optical beams through the filter and synthesize the image; in this case, the point spread function can be viewed.

The simplified design of our optical system is shown in figure 32 and consists of the fiber array at left and focal plane array at right. There are two lenses between which the filters are placed. The optics can be switched between two configurations by simply changing the second lens, which is mounted in a filter wheel to facilitate this. One configuration is a 4-f system that reproduces an image of the source array, while the other is a 6-f system that produces a Fourier transform of the source array. The first configuration is very useful for assisting alignment of the optical filters in the beam path. This is because, as the filter is tilted or translated, the optical power from each channel contributing to the image is immediately apparent from the brightness of the corresponding spot in the image. Thus alignment of the filter is effected by equalizing the brightness of the spots. This arrangement is also useful for characterizing the output of each individual channel in the array. The second configuration produces the imagery corresponding to the scene viewed by the antenna array.
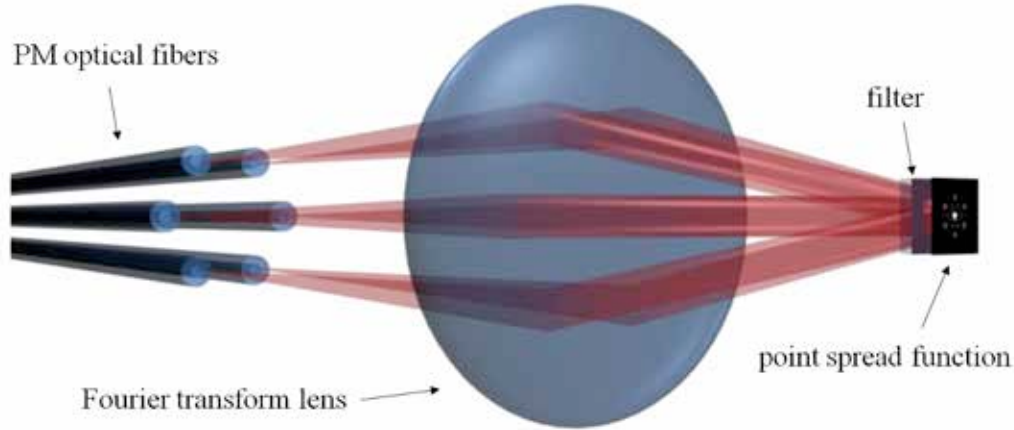
28

Figure 33. Cartoon representation of the basic principle of the image forming optics. The signal captured by each antenna in the array is re-launched by a corresponding optical fiber in an array of the same geometry. A simple lens is used to perform a Fourier transform and synthesize the image. The optical filter is placed about one focal length from the lens in order to pass all of the channels through the limited aperture of the filter. In this case the synthesized image is represented by a six channel point spread function. This image is subsequently relayed to the NIR camera.

The principle of operation of the optical system is shown in cartoon fashion in figure 33. It can be seen that the optical filters are placed near the focal length of the Fourier transform lens. This is because the bundle of optical beams passing through the filter from the entirety of the imager channels is smallest in diameter near this point, such that it fits through limited clear aperture of the filter, as defined by coating uniformity. Put simply, this arrangement is used to maximize the overall carrier suppression that can be achieved by the optical system. On the other hand, it is undesirable to place the filter at exactly the focal length of the lens, because the surface of the filter will then be in focus with the image. As a result, cosmetic defects on the filter surface will be visible in the imagery. The image is produced at the focal length of Fourier transform lens. However, this is not a convenient location for the camera focal plane array because of the location of the filters. Therefore, the image is relayed to another location by the second lens, which is placed two focal lengths away from the image location. The FPA is placed another two focal lengths away from the relay lens. When all of the channels of the imaging system have equal amplitude and phase, the point spread function of the imager is observed, also shown in figure 33. For extended imagery, the amplitude and phase of the channels of the imaging system will vary based on the samples of the Fourier plane by the individual antennas in the array, such that an image of the scene results from their coherent summation.

Because of the relatively weak signal of the optically upconverted sideband compared to the carrier, a large amount of carrier suppression is required. However, the amount of carrier suppression that can be achieved by the optical filter depends on the focal length of the lens used to perform the Fourier transform. This is because the optical beams corresponding to each imager channel pass through the filter at an angle of incidence that increases the further they are off-axis. This presents an effective wavelength to the optical filter that is blue-shifted and hence the transmission properties of the filter depend on the radial location of the channel. As the focal length of the lens is increased, the angle of incidence is reduced, leading to a more uniform filter response for all the channels. This point is illustrated in figure 34, where the effective separation between sideband and carrier is compared for two different focal length lenses.
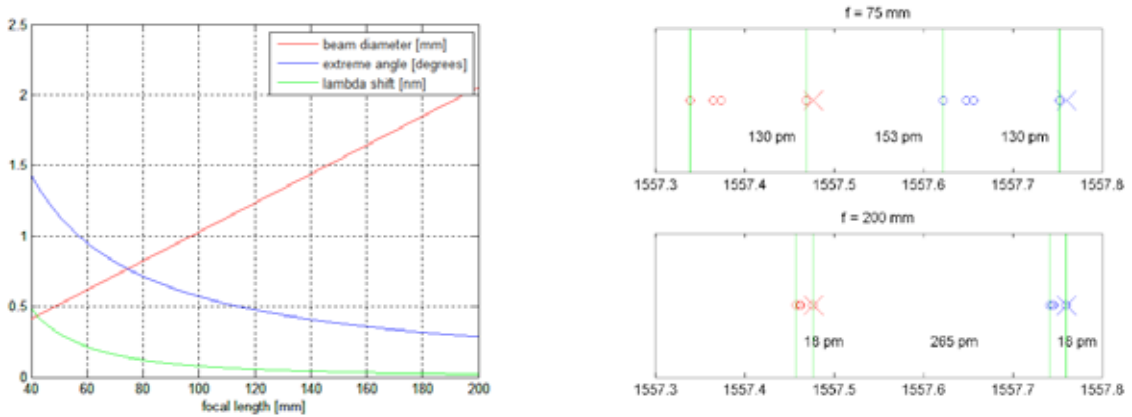
29

Figure 34. Implication of the focal length of the lens used to perform the Fourier transform on beam size and wavelength shift (left). The angle dependence of the wavelength shift results in a range of effective wavelengths passing through the optical filter. As a result, the spacing between carrier and sideband is reduced (right) for short focal length.

A second consequence of the lens focal length is the beam size that results for each channel as it passes through the filter. As the focal length increases, each channel diverges to a larger beam size before being collimated by the lens. Although each fiber is individually collimated by a microlens array, the small beam size means that these beams nonetheless diverge considerably. As such, the individual beams can be several millimeters in diameter before encountering the Fourier transform lens. Therefore the available clear aperture of the filter must be considered when determining the focal length to be used for the lens. It is for this reason that a large aperture area for the optical filter is desirable. This is explicitly shown in figure 34, where it may be seen that increasing the focal length of the lens results in decreased blue-shift for off-axis channels at the expense of an increased beam size and hence a requirement for a larger filter aperture area.
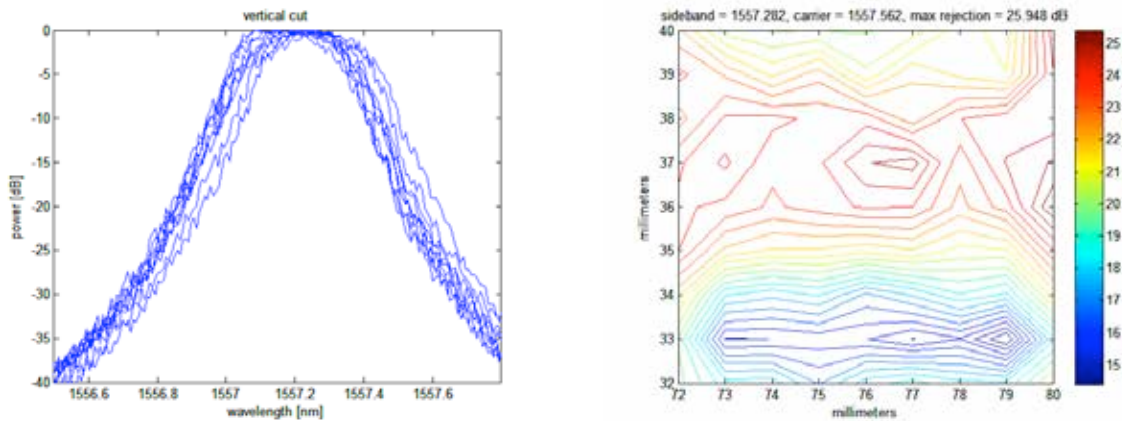

Figure 35. Characterization of the optical filter performance. The 10 x 10 mm filters were measured using an optical spectrum analyzer on a 0.5 mm grid. Measurements taken through along a line through the center of filter are shown (left) along with a contour map of filter rejection (right); about 25 dB of rejection is achieved per filter.

30

We worked with a vendor to procure optical filters at the desired wavelength and with a relatively large clear aperture. Testing results from these filters are shown in figure 35. The filter response was measured on a rectangular grid using an optical spectrum analyzer and computer controlled mechanical stages for positioning. From these measurements, a contour map of carrier suppression was produced, assuming a carrier wavelength of 1557.562 nm and sideband wavelength of 1557.282, corresponding to the lower sideband with 35 GHz operation. Peak carrier rejection near -26 dB was observed, with a relatively uniform area of several millimeters diameter where carrier rejection in excess of -23 dB can be achieved. However, the filters are not normally diced to this large size and therefore custom dicing was performed to produce 10 x 10 mm pieces with the uniform region centered within the piece. We found that the resulting filters had sufficient aperture area to enable a relatively long focal length Fourier transform lens and therefore minimum blue-shift and maximum effective carrier rejection.

Since a single filter does not produce sufficient carrier suppression to realize passive operation of the imager, the filters must be cascaded to increase the sharpness of the filter response. The effect of stacking the filters is indicated in figure 36. Up to four filters are added into the optical path to add progressively more carrier suppression. As seen in the right side of the figure, three filters are sufficient to push the power level of the optical carrier below the level of the passive sideband, while four filters push the carrier entirely into the noise floor of the optical spectrum analyzer used to produce the measurement. Thus sufficient carrier suppression is achieved to detect passive mmW signal levels.
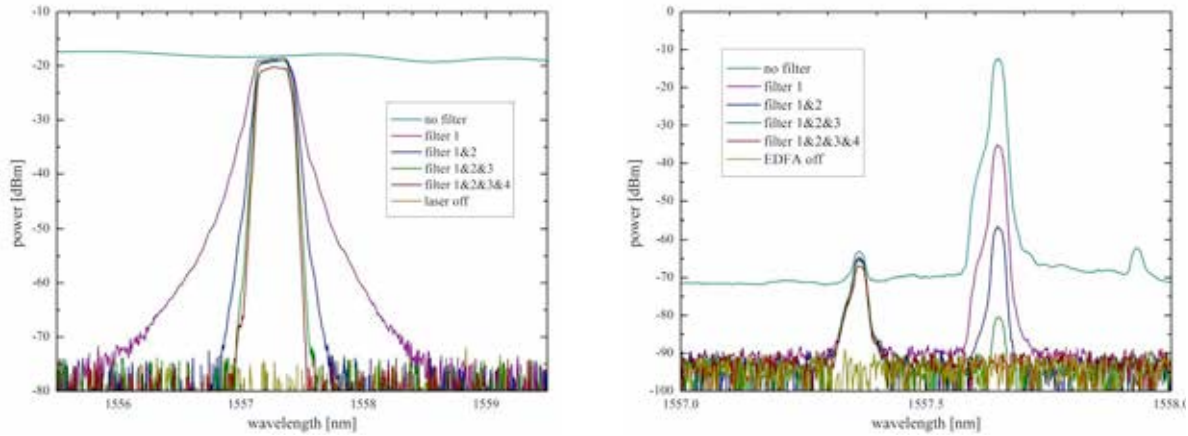

Figure 36. By cascading optical filters, the sharpness of the spectral response is increased (left). A total of four optical filters is sufficient to push the optical carrier into the noise floor (right).

We incorporated the four optical filters into the mmW imager back-end, as shown in figure 36, and subsequently produced point spread function (PSF) measurements that validate the operational specifications of the imager in terms of resolution and field of view. This was accomplished by imaging a Gunn diode operating at 35 GHz. As shown in figure 37, the dual ring hexagonal configuration produced the indicated PSF in ray tracing simulation, which closely matched the experimentally observed PSF. Good agreement is observed, down to the location of the individual sidelobes. An angular resolution of approximately 1 degree and alias-free field of view of 11 degrees were measured. Further system refinement has since led to passive operation of this camera.
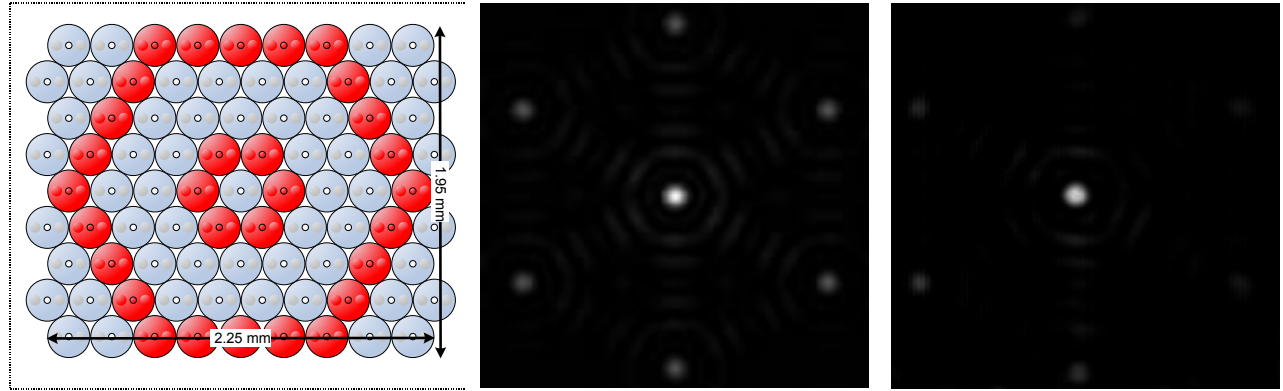
Figure 37. The thirty channel fiber configuration (left) produces the simulated point spread function shown (middle). This is in good qualitative agreement with the measured point spread function (right).

In conclusion, the optical up-conversion technique provides sensitive detection of mmW signals and is amenable to the realization of a distributed aperture imaging system. Such an approach presents a number of advantages as compared to a more conventional direct-detection approach utilizing refractive optics. A key enabler for this technique is the optical filter that is used for suppression of the optical carrier. For reasons discussed in some detail, a large aperture area for the filter is highly desirable. Procurement of such filters has led to the successful demonstration of our passive mmW imaging system.

HIGH SPEED MODULATOR FABRICATION AND PACKAGING
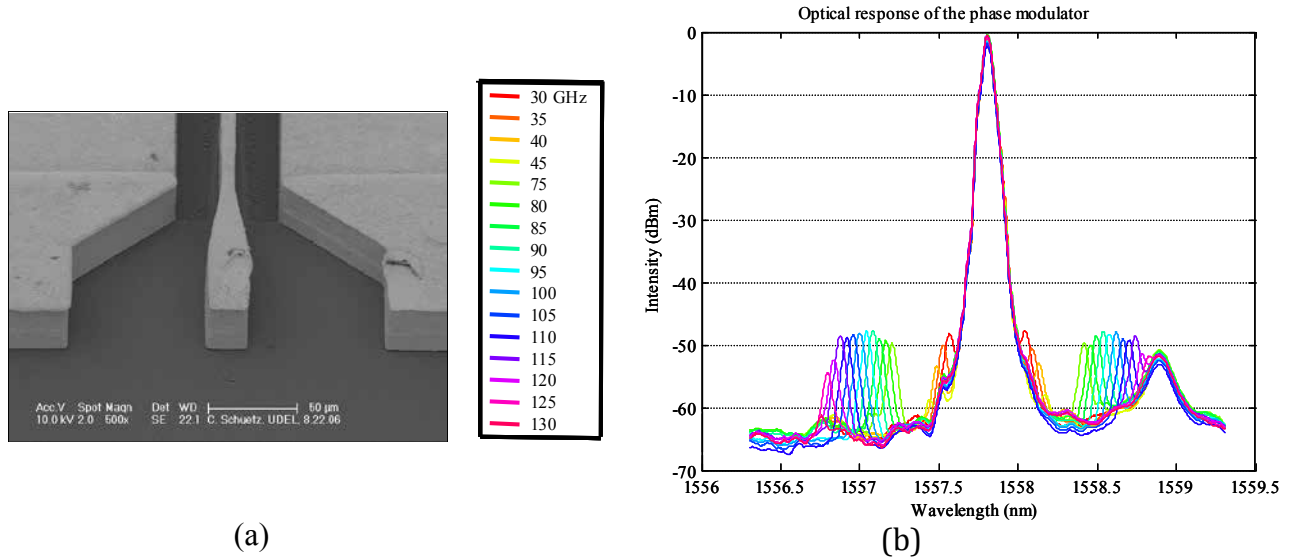

(a)

(b)

Figure 38. Phase modulators fabricated at University of Delaware have demonstrated world record conversion efficiencies at 95 GHz. Shown here are (a) an SEM of the modulator structure showing electrodes and underlying optical waveguide and (b) optical spectra showing modulation sidebands at frequencies up to 130 GHz. Conversion efficiency for modulator shown was measured at world record 0.76 W^{-1} at 95 GHz. Roll-off at 125 GHz is due primarily to power of mmW excitation source.

Considerable benefits can be realized for many applications if the proposed imager could be made to operate at higher frequencies. Both resolution and available passive radiation increase linearly with increasing frequency for a given aperture size. Unfortunately, commercial modulators are only available at frequencies up to ~40 GHz, limiting application of this technique to imaging in the 35 GHz atmospheric transmission window. As part of a recent DARPA program we have successfully developed lithium niobate modulator technologies with operable bandwidths that include the 95 GHz atmospheric window. These modulators, when applied to the distributed aperture imaging approach, would increase the resolution of imager with a given footprint by nearly a factor of three. While these modulators have unparalleled performance in the high frequency regime (see Figure 38), significant effort remains to be able to produce modulators produce modulators suitable for implementation in this imager. The modulators that were previously fabricated were made in a research environment in low volumes and were not packaged. To realize these modulators for imaging applications, manufacturing and packaging schemes must be realized.
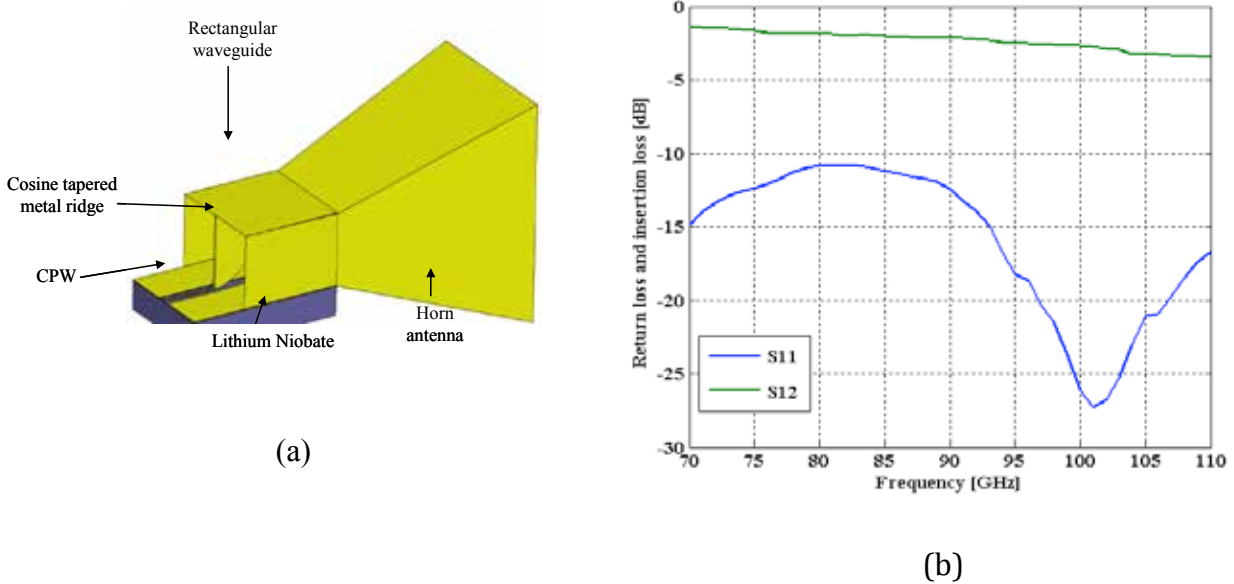

(a)

(b)

Figure 39. Adiabatic fin transition from waveguide-to-CPW shown schematically in (a) allows broadband, low-loss coupling of millimeter-wave radiation in the W-band with simple integration techniques. Simulations of this junction have shown very loss transmission and return losses across the full W-band as shown in (b).

Commercial modulators have established fairly standard practices for the packaging of modulators up to 40 GHz, which, for the most part can be adopted to package the high-frequency modulators. However, current packaging techniques utilize coaxial connectors, which are standardized up to 67 GHz. Emerging connectors should push this to 110 GHz, but the majority of millimeter-wave components in this frequency range use rectangular waveguide. So for ease of implementation for these imagers it would be desirable to package the modulators with a waveguide coupled interface.

To this end, we have developed a design that will allow low-loss coupling of the modulator coplanar waveguide (CPW) to a conventional WR-10 rectangular waveguide across the full W-

band (75-110 GHz) as shown in Figure 39. The morphology of this transition is amenable to simple pick-and-place alignment of the waveguide transition to the modulator surface. As such, with the development of appropriate packaging tools and die, the modulators can be waveguide coupled in high volumes with low cost. Under this effort, we have experimentally realized such a waveguide transition and incorporated it into a packaged device as shown in Figure 40.
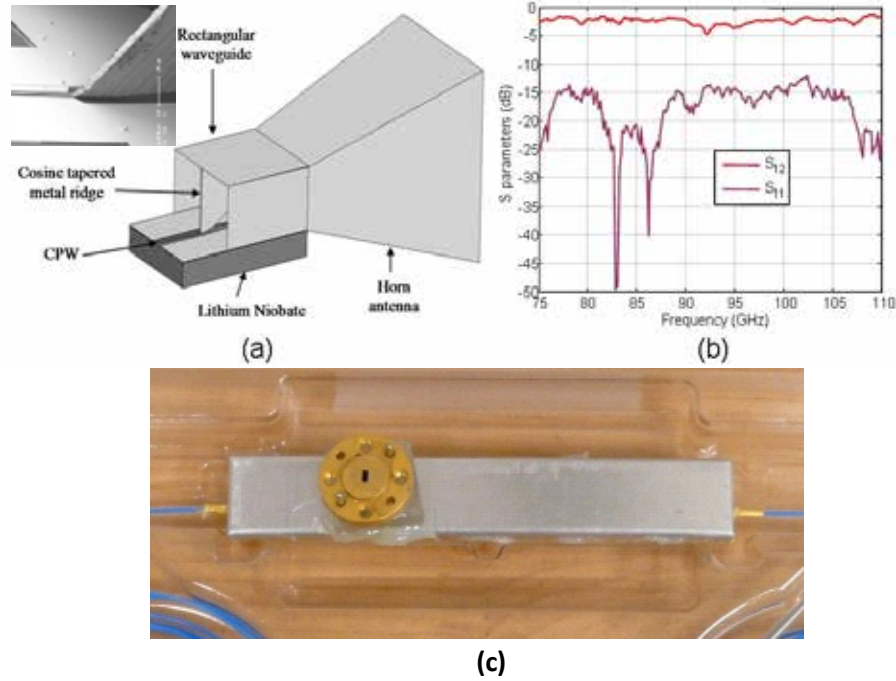

(a)

(b)

(c)

Figure 40. Packaging of modulator chip. (a) Schematic of fin-coupled transition mechanism for CPW-WR10 integration. The inset SEM micrograph shows contact between taped fin structure and CPW. (b) Experimental results of return loss and insertion loss of the fin-coupled integration. (c) Photograph of fully packaged modulator in a sealed metal housing with optical fiber bonding and WR-10 integration.

This transition was incorporated into a fully packaged modulator including optical fiber, WR-10 coupling and protective housing. For optical bonding, the modulator chip was first polished at both end faces, and then bonded to PM fibers that has been pre-positioned in silicon V-grooves. Insertion loss of 5.5dB was obtained. Coupling to WR-10 rectangular waveguide was realized using a fin-coupled transition mechanism, as shown in Fig. 40(a). The fin protrudes down from the waveguide top and touches the signal electrode at its tapered end. The fin structure allows that electric field smoothly transfers from waveguide mode to CPW mode. As a result, -3.5 dB insertion loss at 94 GHz was achieved, as shown in Fig. 40(b). Figure 40(c) shows the fully packaged modulator in a sealed metal housing.

Two of these modulators were fabricated and installed in the single pixel imager described above. This imager yielded W-band millimeter-wave imagery that was used for some of the first ever phenomenology and perception studies performed at these wavelengths. Some sample imagery from these studies is shown previously in Figures 5 and 6.

34

SYSTEM INTEGRATION AND TEST

Under this effort we also began testing the characteristics of the array as built at the start of this effort, which consisted of the dual concentric hexagons and is described in more detail in the distributed aperture imaging section above. A number of possible configurations within this array were tested experimentally and used to validate simulated results and experimental performance. Overall excellent agreement was achieved showing both the validity of the simulation model and the operation of the hardware and phase control loops.

The point spread function (PSF) for different arrangements of various numbers of millimeter wave receivers was simulated to choose a desired configuration. The PSF (sometimes referred to as the system's impulse response) describes the response of an imaging system to a point source or point object. In functional terms it is the spatial domain version of the modulation transfer function (MTF). The degree of spreading (blurring) of the point object is a measure for the quality of an imaging system. In incoherent imaging systems the image formation process is linear meaning that when two objects A and B are imaged simultaneously, the result is equal to the sum of the independently imaged objects. A dual hexagonal ring configuration with 6 inner and 24 outer detectors was chosen as a starting point (Figure 41). This configuration closely approximates the Kogan ring configurations used for snapshot imaging in the radio astronomy community. This implementation has a maximum baseline of 400 mm, a minimum baseline of 50 mm, with a simulated alias free FOV of 11.65 degrees and a FWHM resolution of 1.07 degrees at 35 GHz. The configuration, simulated PSF, and measured PSF are shown in Figure 41. The measured PSF was performed using a 35 GHz Gunn diode placed several meters away. The distributed aperture configuration allows for electronic scanning and focusing by adding the proper phase to each channel. The inherent phase errors were calibrated out of the system and the imager was focused at the Gunn diode distance. There is excellent spatial agreement between the measured performance and the simulation (Figure 42). By simply turning off every other channel it is easy to show the effect of a doubling of the minimum baseline on the FOV (Figure 43). Similarly, by turning off the outer 24 channels it is easy to show the effect the maximum baseline has on the resolution (Figure 44).
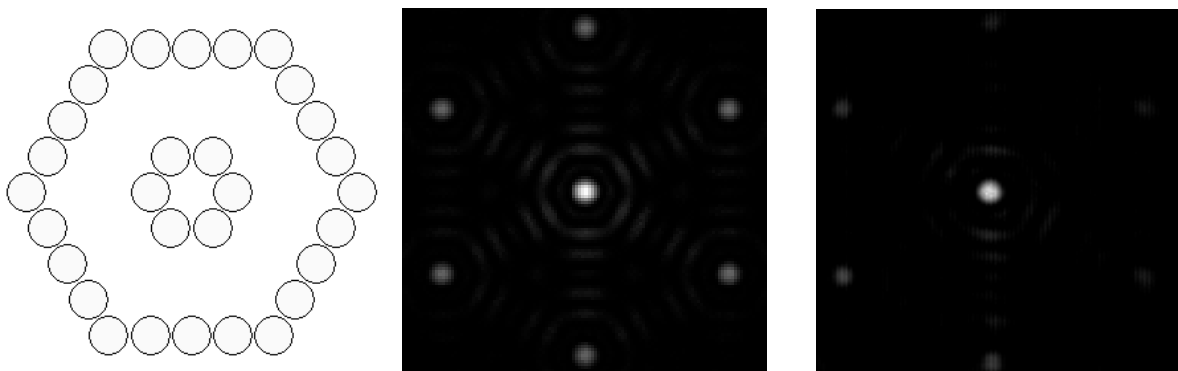

Figure 41. Channel placement for 30 channel, 35 GHz distributed aperture imaging system (left), simulated PSF for ±12 degree FOV (center), and measured PSF (right).
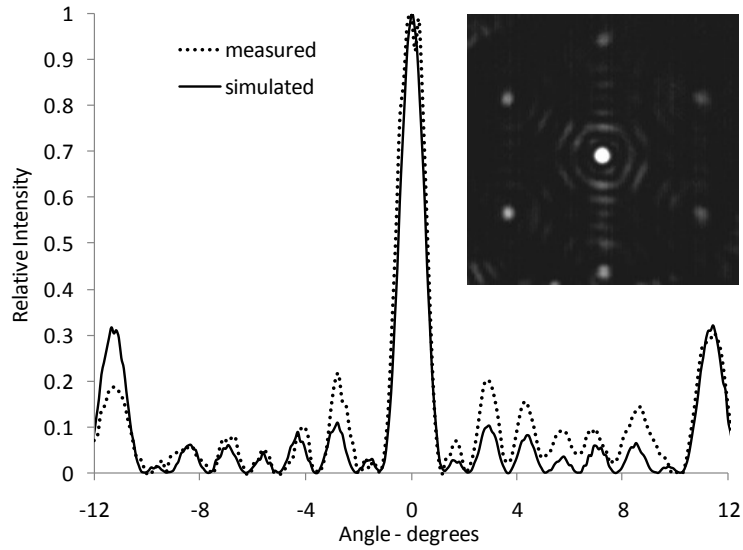
Figure 42. Comparison of vertical cross sections of the simulated and measured PSF. The measured PSF is shown as an inset where the brightness and contrast have been adjusted to show the background patterns.
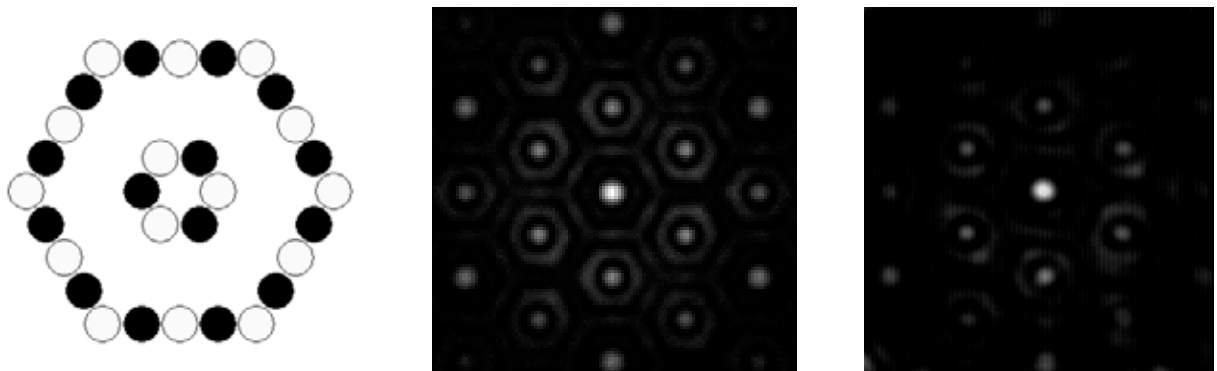

Figure 43. Channel placement for 15 channel, 35 GHz distributed aperture imaging system where the black circles indicate the channel is turned off (left), simulated PSF for ±12 degree FOV (center), and measured PSF (right). Notice that doubling the minimum baseline results in halving the alias free field of view.
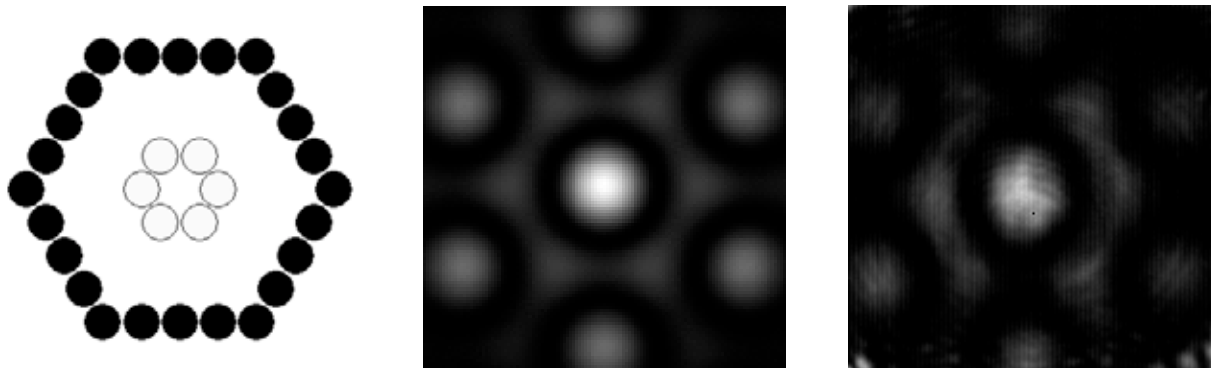

Figure 44. Channel placement for 6 channel, 35 GHz distributed aperture imaging system where the black circles indicate the outer ring of detectors is turned off (left), Simulated PSF for ±12 degree FOV (center), and measured PSF (right). Note that reducing the maximum baseline decreases the resolution of the imager.
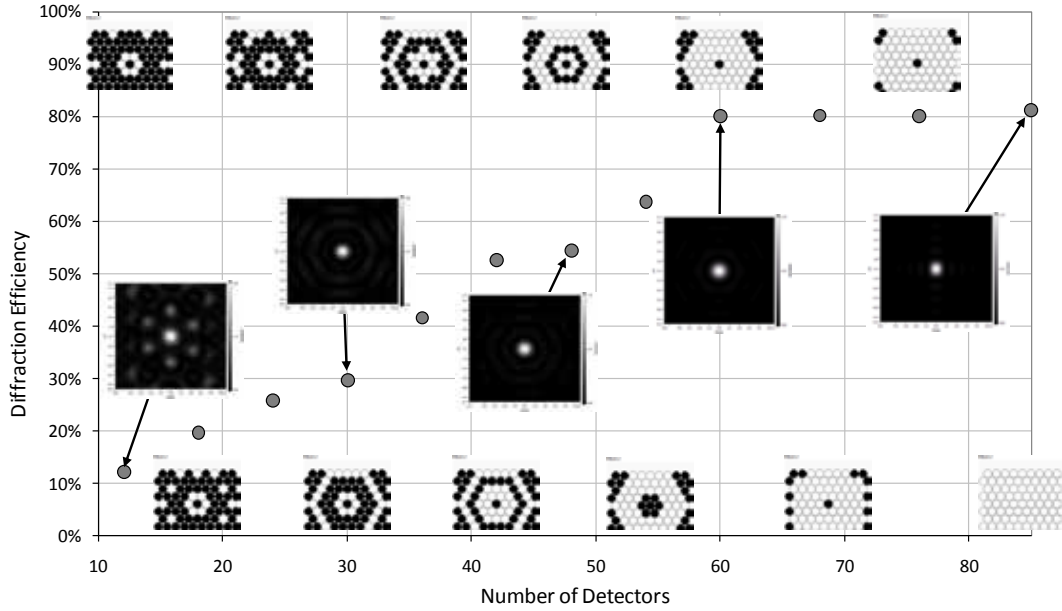
Figure 45. Simulated diffraction efficiency versus number of elements for various configurations of a 35 GHz distributed aperture imaging system for ± 5.5° FOV. Simulated PSFs are shown for some of the configurations.

In addition, these simulation models were utilized to determine diffraction efficiency of the various array layouts possible with the available fiber array. Diffraction efficiency is a measure of the ratio of energy in the main image forming spot of the imager PSF to the overall energy in the PSF. A plot of diffraction efficiency is shown in Figure 45 for a number of array layouts. As expected diffraction efficiency generally increases with a larger number of elements.

CONCLUSION

Under this effort we have demonstrated significant progress in a number of component areas required for the realization of optically-enabled, passive millimeter-wave imagers. While this progress was made in many widely disparate and often seemingly unrelated areas, each of these elements is essential to the realization of the proposed distributed aperture arrays with arbitrary array layouts. There arbitrary arrays will be essential for the realization of wide field of view imagers with low distortion due to aliasing and sidelobes in the PSF of the array. We have also made significant progress in the fabrication of the narrowband filters with wide physical areas and the optical configurations required to leverage these filters. Such filtering is also essential to the realization of low noise imagery using this technique. Finally, we have demonstrated significant progress in the packaging of W-band optoelectronic modulators, which have been utilized in phenomenology studies using a single-pixel imaging scanner. This modulator packaging technology will be utilized to increase the accessible bandwidth of imagers utilizing the optical upconversion approach, thereby increasing the resolution that can be achieved from a given aperture size.